

UC San Diego

UC San Diego Electronic Theses and Dissertations

Title

Collagen's Role in the Dermal Armor of the Boxfish

Permalink

<https://escholarship.org/uc/item/3t76x1s5>

Author

Garner, Sean N

Publication Date

2018

Peer reviewed|Thesis/dissertation

UNIVERSITY OF CALIFORNIA SAN DIEGO

Collagen's Role in the Dermal Armor of the Boxfish

A Thesis submitted in partial satisfaction of the requirements for the degree Master of Science

in

Materials Science and Engineering

by

Sean Nolan Garner

Committee in charge

Professor Joanna M. McKittrick, Chair
Professor Shengqiang Cai
Professor Marc Meyers

2018

The Thesis of Sean Nolan Garner is approved and it is acceptable in quality and form for publication on microfilm and electronically:

Chair

University of California San Diego

2018

Dedication

Thank you for teaching me the significance of light-heartedness and comradery. Your contagious passion and giving nature have left me inspired to do good, whether big or small. You shocked everyone around you with your ability to bring people together. To my beloved friend, Kenneth Yun (1994-2017).

Table of Contents

Signature Page	iii
Dedication	iv
Table of Contents	v
List of Figures	vii
Acknowledgements	x
Abstract of the Thesis	xi
1 Introduction.....	1
2 Background	7
2.1 General Information and Phylogeny of Boxfish.....	7
2.2 Scute Structure	8
2.3 Collagen Structure.....	14
2.3.1 Heirarchical Structure of Collagen Fibrils	14
2.3.2 Small Angle X-ray Scattering	17
2.3.3 The Bouligand-type Structure	20
2.3.4 The Nested-bowl Structure	26
2.4 Mechanical Characterization.....	27
3 Hypothesis.....	30
4 Materials and Methods	31
4.1 Confocal Microscopy	31
4.2 Micro-Computed Tomography	31

4.3 Nanoindentation	31
4.3.1 Nanoindentation Data Analysis	32
4.4 In-situ Scanning Electron Microscopy.....	34
4.5 In-situ Small Angle X-ray Scattering	34
5 Results and Discussion.....	37
5.1 Confocal Microscopy.....	37
5.2 Micro-Computed Tomography	39
5.3 Nanoindentation	42
5.4 In-situ Scanning Electron Microscopy.....	43
5.5 Small Angle X-ray Scattering	48
6 Applications and Bioinspiration.....	53
7 Conclusions	58
7.1 Recommendations for Future Research	60
Appendix.....	62
Appendix A. Staining Protocol	62
Appendix B. Rehydration of Boxfish Scutes Protocol	64
References.....	65

List of Figures

Figure 1.	Various dermal armors of fishes.	1
Figure 2.	The <i>Arapaima gigas</i> employs a natural dermal armor to protect against predators, including the piranha. Figure adapted from [2].	2
Figure 3.	Examples of Bouligand-type structure found in nature. Figure adapted from [3,5].	3
Figure 4.	Bioinspired additive manufacturing (robocasting) of alumina platelets into fibers with and without a Bouligand-type structure in in-situ double cantilever beam testing. Figure adapted form [6].	4
Figure 5.	Image of the beetle <i>C.gloriosa</i> which exhibits iridescence as a result of its Bouligand structure. Figure adapted from [9].	5
Figure 6.	Image of biotemplated crustaceous chitosan hydrogel that changes color in response to change in the pH of its solvent. Figure adapted from [8].	6
Figure 7.	Maximum likelihood phylogenetic hypothesis of boxfish. Figure adapted from [7].	7
Figure 8.	Vorticity patterns during 20° pitch angles of two differently shaped boxfish species: (a) <i>R. triqueter</i> and (b) <i>O. cubicus</i> . Image taken from [9].	8
Figure 9.	Micro-computed tomography images of the boxfish, <i>Lactoria cornuta</i> . (a) Perspective view; (b) Ventral view; (c) Sinister view; (d) Anterior view. Scale bars: (a–d) 5 mm. Figure adapted from [6].	9
Figure 10.	Various sutured interfaces found in biological materials. Figure adapted from [14].	10
Figure 11.	Schematic of mineralized plates and walls that make up a boxfish scute. Figure adapted from [4].	11
Figure 12.	Three types of honeycomb sandwich structures: (a) hexagonal honeycomb, (b) square honeycomb and (c) triangular honeycomb. Figure adapted from [20].	12
Figure 13.	Examples of bioinspired sandwich composites. Figure adapted from [22,23].	14
Figure 14.	Ashby plot revealing the differences in toughness (fracture energy) and stiffness (Young’s modulus) among biomaterials made from collagen and hydroxyapatite. Figure adapted from [24].	15
Figure 15.	Hierarchical assembly of collagen fibrils. Figure adapted from [25].	16
Figure 16.	Hierarchical assembly of bone and its deformation response to tensile load at the tissue level, fibril array level, and mineralized collagen fibrils. Figure adapted from [26].	17
Figure 17.	Small-angle X-ray scattering (SAXS) diffraction pattern from <i>Arapaima gigas</i> scales. Figure adapted from [2].	19
Figure 18.	<i>In-situ</i> small-angle X-ray scattering (SAXS) analysis on <i>A. gigas</i> scale collagen structure. Figure adapted from [2].	20
Figure 19.	(a) Plywood structure with 90° rotation of fibrils in each layer. (b) Twisted plywood structure with a small angle rotation between each equidistant layer. When observed through an oblique slice the structure reveals its characteristic arcs. Figure adapted from [4].	21

Figure 20.	Examples of animals that contain Bouligand-type structures. Figure adapted from [5,37,38].	23
Figure 21.	(a) Top view of mineralized surface of boxfish (<i>Lactoria cornuta</i>); (b), (c) Scanning electron microscopy of top view with mineral plate removed revealing an apparent ladder-like structure. Scale bars: (a) 500 μm ; (b) 100 μm ; (c) 5 μm .	24
Figure 22.	Scanning electron microscope (SEM) image of the cross-section of the exoskeleton of the cuticle in a lobster <i>Homarus americanus</i> . Figure adapted from [41].	25
Figure 23.	Transverse section of boxfish scute using optical microscopy between crossed polar. Figure adapted from [4].	25
Figure 24.	The nested-bowl structure found in the scute of the boxfish (). (a) Simplified schematic of collagen structure in boxfish scute; (b) Confocal microscope image of cross-section of boxfish scute revealing the nested-bowl structure. (a) adapted from [4].	27
Figure 25.	Tensile stress-strain results of two connected boxfish (<i>Lactoria cornuta</i>) scutes. Both wet and dehydrated samples were tested with the wet samples exhibiting a lower elastic modulus. Figure adapted from [6].	28
Figure 26.	Shear stress-shear strain results of two connected boxfish (<i>Lactoria cornuta</i>) scutes. Both wet and dehydrated samples were tested. Large variance in data due to different samples having significant differences in the number of teeth interlocking and subsequently failing. Figure adapted from [6].	29
Figure 27.	(a) Schematic of the punch test experiment with array of boxfish scutes; (b) Penetration test results on boxfish (<i>Lactoria cornuta</i>) scutes. Figure adapted from [6].	29
Figure 28.	Hydrated nanoindentation was performed using a TI 950 TriboIndenter (Hysitron, USA) on the top side of a boxfish scute with its mineral plate carefully removed from polishing.	32
Figure 29.	Generalized schematic of a nanoindentation procedure. Figure adapted from [44].	33
Figure 30.	Experimental set-up of the <i>in-situ</i> scanning electron microscopy mechanical loading in both tension (left) and shear (right). Two neighboring scutes are held on opposing sides and imaged using SEM before and after the deformation take place.	34
Figure 31.	Representative example of <i>in-situ</i> small angle X-ray scattering performed on boxfish scute.	36
Figure 32.	Confocal microscopy top view of the collagen in a boxfish scute.	37
Figure 33.	Confocal microscopy image of boxfish scute cross-section.	38
Figure 34.	Confocal microscopy image of boxfish scute oblique cross-section.	39
Figure 35.	Micro-computed tomography images of boxfish scutes.	40
Figure 36.	(a) Scute model with highlighted region representing approximate location of the micro-computed tomography (μ -CT) 3D images; (b) Cross sections of 3D μ -CT images showing Bouligand-type structure.	41

Figure 37.	Nanoindentation was performed on the top of a boxfish scute with its mineral plate carefully removed from polishing.....	43
Figure 38.	<i>In-situ</i> scanning electron microscopy images with the mineralized plate under: (a) and (b), tensile loading and (c) and (d), shear loading.....	44
Figure 39.	<i>In-situ</i> scanning electron microscopy images with the mineralized plate removed, loaded in (a) tension and (b) shear. Regardless of the loading mode, failure occurs almost entirely at the interface.....	45
Figure 40.	Close-up <i>in situ</i> scanning electron microscopy images before and after shear loading.	46
Figure 41.	Scanning electron micrograph of neighboring boxfish scutes with mineral plates removed. A periodic crack on left-side scute can be observed which is representative of the periodic Bouligand-type structure of the collagen.....	47
Figure 42.	Scanning electron micrograph of crack in the mineral plate of a boxfish scute. Tubules with uncharacterized material extending out.....	48
Figure 43.	<i>In-situ</i> small angle x-ray scattering patterns obtained from a top-down scan in between two neighboring boxfish scutes before undergoing deformation.....	49
Figure 44.	<i>In-situ</i> scanning electron microscopy of the collagen fibers at the interface between neighboring boxfish scutes after tensile loading.....	50
Figure 45.	(a) Stress-strain data for the tensile test with two neighboring boxfish scutes with mineral plate removed; (b) Shear stress-shear strain data for the shear test with two neighboring scutes. Significantly higher strains are observed in the shear data, as compared to the tensile data.	51
Figure 46.	Fibril strain (obtained from <i>in-situ</i> SAXS) versus overall tissue strain (obtained from digital image correlation) of the interfacial collagen between two neighboring boxfish scutes during tension, (a), and shear, (b).....	52
Figure 47.	(a) Mosaic art from about the fourth century B.C. depicting soldiers in Lorica Squamata armor. (b) Archaeological artifact of the Lorica Squamata armor. Images adapted from [45].	53
Figure 48.	3D printing of Bouligand-type structural materials through combination of stereolithography and ultrasound directed self-assembly. Figure adapted from [50]	55
Figure 49.	Schematic diagram of the electrically assisted 3D printing platform, (a), for synthesis of Bouligand-type nanostructures with surface modified multiwall carbon nanotubes (MWCNT-S). Figure adapted from [51].....	56
Figure 50.	Biotemplating of stone crab shell with Bouligand-type structure [52].	57

Acknowledgements

I would like to acknowledge Professor Joanna McKittrick for her support as the chair of my committee, and for her guidance with this research.

This thesis, in full, is currently being prepared for submission for publication of the material. Garner, Sean; Naleway, Steven; Housseini, Maryam; Acevedo, Claire; Gludovatz, Bernd; Schaible, Eric; McKittrick, Joanna; Zavattieri, Pablo.

I would also like to acknowledge the contributions of the following individuals: Professor Philip Hastings of the Scripps Institution of Oceanography for providing me with boxfish samples for testing; Dr. Eric Bushong from the National Center for Microscopy and Imaging at UC San Diego for assisting me with performing μ -CT with my samples; Professor David Kisailus and Dr. Nick Yaraghi for allowing me to use their nanoindentation apparatus. Finally, I would like to thank the members of Professor McKittrick's research lab for their guidance and expertise.

This work has been made possible by the Multi-University Research Initiative through the Air Force Office of Scientific Research (AFOSR-FA9550-15-1-0009).

ABSTRACT OF THE THESIS

Collagen's Role in the Dermal Armor of the Boxfish

by

Sean Nolan Garner

Master of Science in Materials Science and Engineering

University of California San Diego, 2018

Professor Joanna M. McKittrick, Chair

This thesis aims to further the understanding on the structure and mechanical properties of the dermal armor of the boxfish (*Lactoria cornuta*). Structural differences between collagen regions underlying the hexagonal scutes were observed with confocal microscopy and microcomputed tomography (μ -CT). μ -CT revealed a tapering of the mineral plate from the center of the scute to the interface between scutes, suggesting the structure allows for more flexibility at the interface. High-resolution μ -CT revealed, for the first time, a 3D image of the dermal armor's complex collagen structure. Helical interfibrillar gaps in the collagen base were found that are structurally similar to micron-sized canals found in the twisted plywood, or Bouligand-type, structure of the lobster, *Homarus americanus*; thereby, suggesting the collagen

in the boxfish is also of a Bouligand-type structure. Nanoindentation further corroborates a Bouligand-type structure by mapping the hardness and reduced modulus of the collagen along the helical axis. Lastly, *in-situ* scanning electron microscopy and small-angle X-ray scattering tests were performed in shear and tension between two connected scutes. Final failure occurred at the interfacial collagen with all tests, suggesting that this region is structurally designed to preferentially absorb energy during deformation to protect the internal collagen. These findings further the understanding of the structure and mechanics of the dermal armor of the boxfish which help provide a basis to synthesize bioinspired composites for impact-resistant materials, specifically with bioinspired Bouligand-type structures to create novel fiber-reinforced composites.

1 Introduction

Biological materials continue to provide the field of materials science great inspiration due to the plethora of material properties billions of years of evolution has provided. For example, biological materials overcome traditional tradeoffs encountered with synthetic materials, such as that of flexibility with strength (e.g. wood) and stiffness with density (e.g. bone). In the past few decades, materials scientists and engineers have been exploring the structure and mechanics of various dermal armors in fish due to their ability to defend against predator's bites while maintaining enough flexibility to efficiently maneuver their environment, as well as other interesting properties like anti-biofouling and reduced drag [1]. Examples of these dermal armors in fish can be seen in Figure 1.

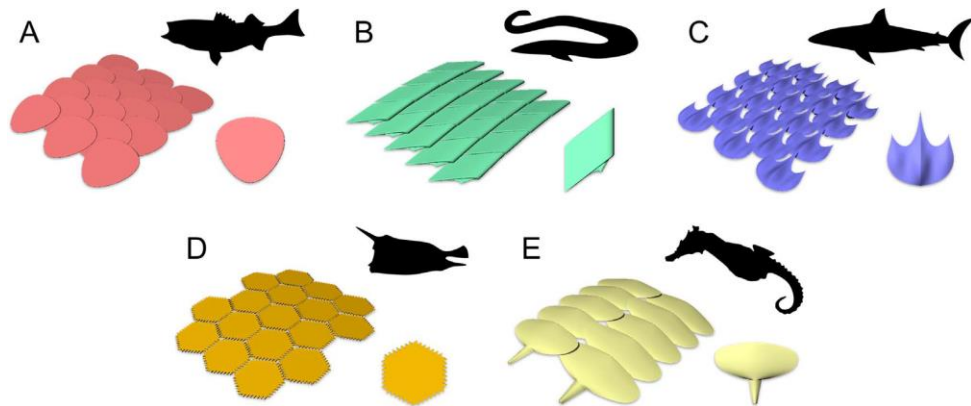


Figure 1. Various dermal armors of fishes. (A) Overlapping elasmoid scales seen in teleost fish, such as the striped bass; (B) interlocking ganoid scales found in gars; (C) partially imbricated placoid scales seen in sharks – display anti-biofouling and reduced drag properties; (D) hexagonal carapace scutes with interdigitated interfaces seen in boxfishes; (E) interlocking bony plates seen in syngathid fishes such as the seahorse. Figure adapted from [1].

Aside from the scale geometry and overall layout, the structure of the individual scales or scutes also plays a vital role in the overall performance. For example, elasmoid scales are thin, lightweight, and flexible scales found in teleost fish. Although the elasmoid scales have a less robust structure compared to other types of scales (e.g. ganoid), they employ a gradient of mineralization and hardness throughout the thickness of the scales to ensure they still resist penetration from predators' bites from the top region and resist bending forces through its ductile lower region. Recent studies on the *Arapaima gigas* (Figure 2), a fish with elasmoid scales, have analyzed this compliant region, or inner lamellar layer, and found that the structure consists of 50 μm thick layers of uniaxial mineralized collagen fibrils, as seen in Figure 2c [2].

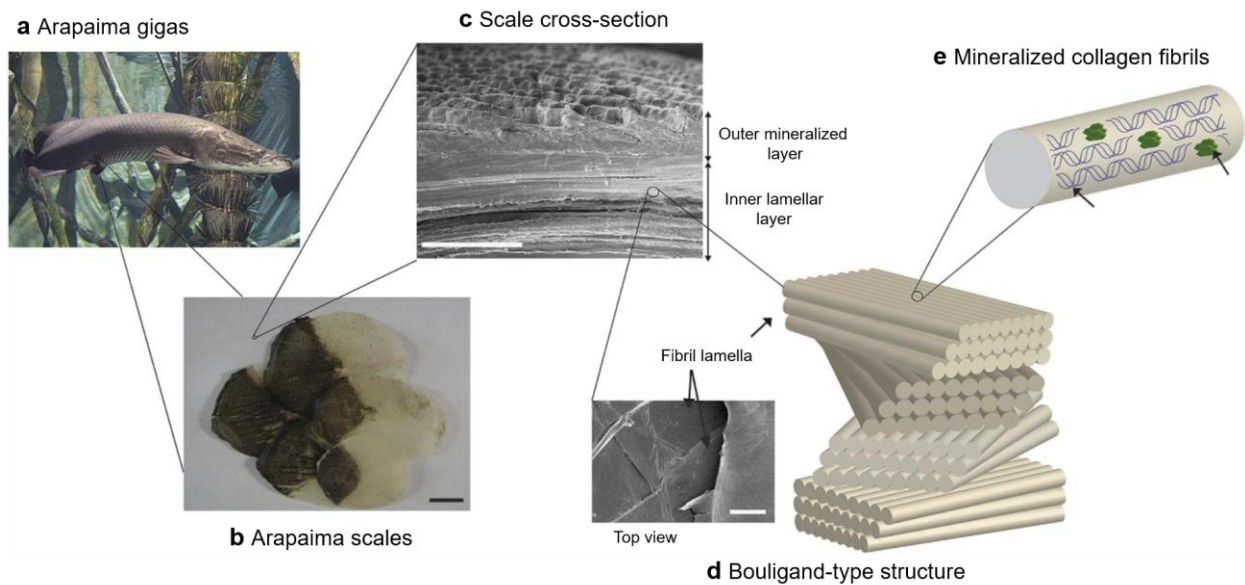


Figure 2. (a) The *Arapaima gigas* employs a natural dermal armor to protect against predators, including the piranha; (b) Overlapping elasmoid scales (scale bar, 20 mm); (c) Cross section of scale showing its graded structure and the periodicity in the inner lamellar layer (scale bar, 0.5 mm); (d) Twisted plywood, or Bouligand-type, structure found in the inner lamellar layer (scale bar, 200 μm); (e) The individual mineralized collagen fibril making up of the Bouligand-type structure. Figure adapted from [2]

Between each layer the alignment of the fibrils is periodically offset which creates a twisted-plywood structure, referred to as a Bouligand-type structure (Figure 2d), which is seen in many

other impact resistant biological materials like the exoskeletons of arthropods, the dactyl club of the mantis shrimp, and in the collagen base of boxfish scutes (Figure 3) [3-5]. Experimentation and simulations on biomimetic Bouligand-type structures have been promising, as the structure displays several advantageous properties. These advantages include: (1) creating quasi-isotropic fiber reinforced materials to avoid weakness in a given axis; (2) allows for the fibers to reorient along the loading axis to provide more resistance; (3) improved energy dissipation and stress relaxation by influencing cracks to follow the helical fiber orientations; thereby, maximizing crack surface area per unit volume [2,3].

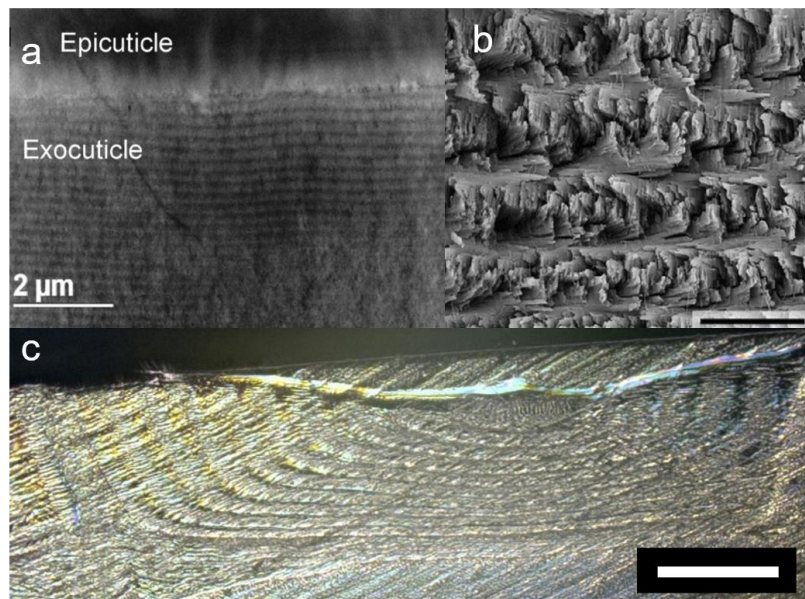


Figure 3. Examples of Bouligand-type structure found in nature: (a) STEM image of Bouligand-type structure found in the exocuticle of a *Cotinis mutabilis* beetle with estimated half-period (layer thickness) of 220 nm. (b) SEM micrograph of the periodic region of an *Odontodactylus Scyllarus* (mantis shrimp) with Bouligand-type structure with an estimated half-period of $\sim 15 \mu\text{m}$; (scale bar, $20 \mu\text{m}$) (c) Confocal microscope image of cross-section of *Lactoria cornuta* (boxfish) scute showing the nested-bowl structure of Bouligand-type microstructure (scale bar, $500 \mu\text{m}$). It is noted that the periodicity and ultra-structural layout of Bouligand-type structures in nature are shown to vary significantly. Figure adapted from [3,5].

The Bouligand structure continues to prove itself through recent works published on bioinspired self-assembly, additive manufacturing, and biotemplating. [6-8] Furthermore, these resultant materials also include ceramic fiber composites (Figure 4), demonstrating the far-reaching potential this biological structure has to offer to fibrous composites of nearly any material. Bioinspired Bouligand-type structures are also promising photonic materials as their long-range order selectively reflects polarized light based on the pitch twisting structure.

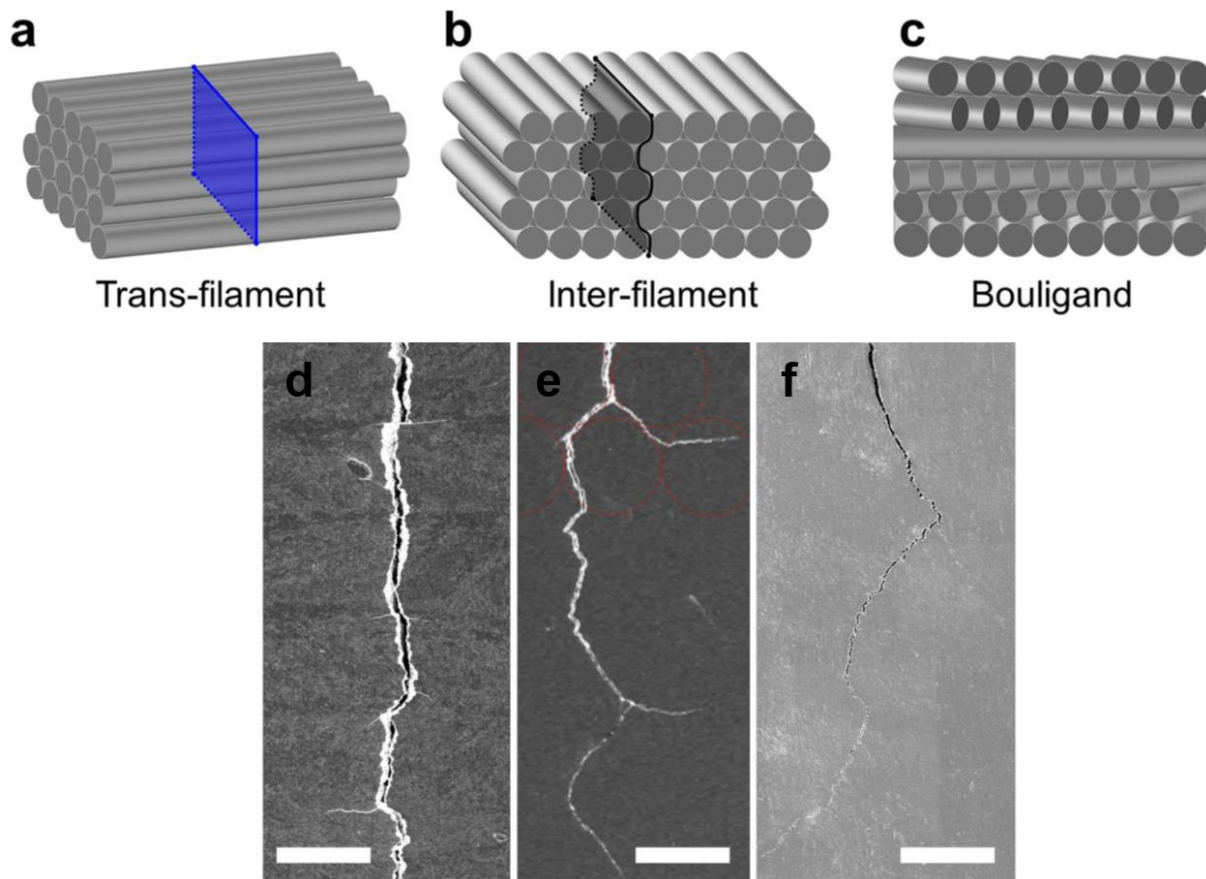


Figure 4. Bioinspired additive manufacturing (robocasting) of alumina platelets into fibers and comparing the difference between crack propagation in the overall ceramic-polymer composite with and without a Bouligand-type structure through *in-situ* double cantilever beam testing; (a) and (d) demonstrate the model and *in-situ* snapshot of trans-filament crack propagation; (b) and (e) demonstrate interfilament crack-propagation and deflection; (c) and (f) demonstrate crack deflection in the Bouligand-type structure. Overall, deflection is seen in both interfilament and Bouligand arrangement but the advantage of the Bouligand structure is that it rotates the crack plane about the in-plane axis. Figure adapted form [6].

Biological examples of this can be seen from the resultant iridescence of beetles, as shown in Figure 5. Researchers have been exploring how to take advantage of both the tough and photonic properties of the Bouligand structure to develop novel materials.

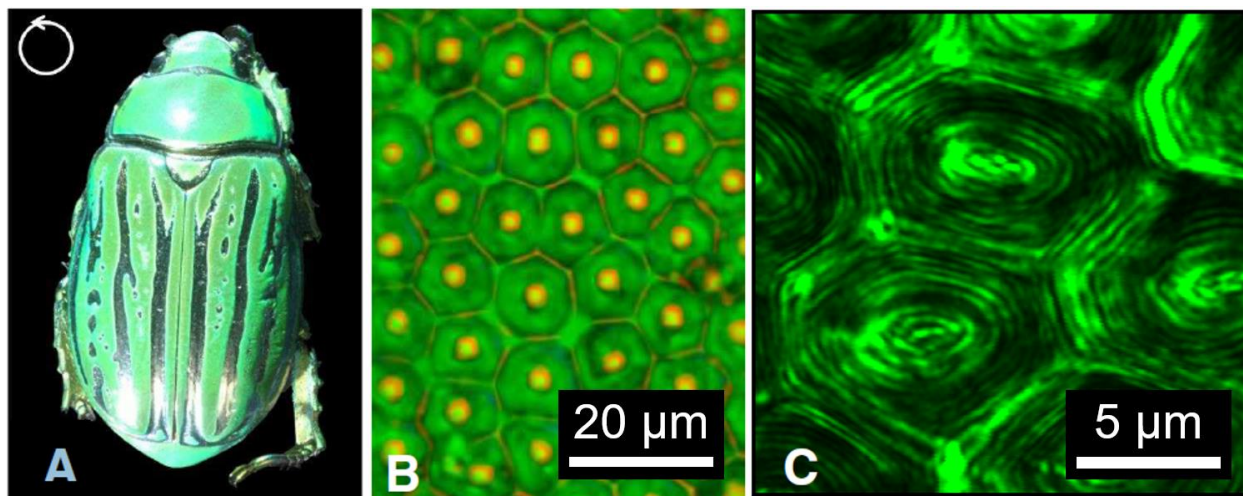


Figure 5. (a) Image of the beetle *C.gloriosa* which exhibits iridescence as a result of its Bouligand structure; (b) Reflected light microscope image further revealing the polygonal cell structure of the brightly colored exoskeleton; (c) Confocal light microscope image demonstrating the concentric rings present on the free surface of the cells. Figure adapted from [9].

For example, Bharath Natarajan et al. [7] were able to successfully design a strong and tough cellulose nanocrystal (CNC) photonic film through a self-assembly process using a combination of CNC derived from both wood and tunicates. Another example from Thanh-Dinh Nguyen et al. [8] utilize a biotemplating process on crustacean shells, which already possess the Bouligand structure, to produce photonic hydrogels composed of chitosan nanofibrils. These hydrogels can swell in response to a change in the solvent environment which, in turn, produce different colors, as shown in Figure 6. These examples are evidence that continuing to produce bioinspired materials based on the Bouligand structure will produce a myriad of materials with exceptional mechanical and optical properties and also stress the importance of studying other Bouligand-

type structure found in biological organisms not yet fully analyzed by materials scientists and engineers.

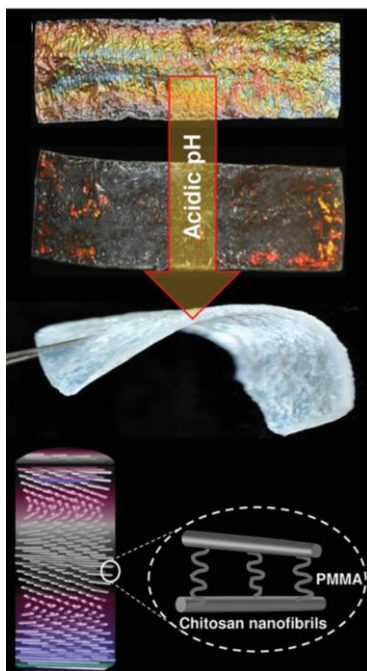


Figure 6. Image of biotemplated crustacean chitosan hydrogel that changes color in response to change in the pH of its solvent. Figure adapted from [8].

This thesis aims to look deeper into the complex structure of the underlying collagen in the armored carapace of the boxfish which appears to have a Bouligand-type structure. The boxfish scutes employ a similar layout to that of the *Arapaima gigas* scales by utilizing a mineralized hydroxyapatite ($\text{Ca}_{10}(\text{PO}_4)_6(\text{OH})_2$) plate to resist penetration and a Bouligand-type structure in its collagen (mainly type I) base to provide toughness [10]. However, as first revealed by Besseau and Bouligand [4], the collagen base consists of a unique nested-bowl macrostructure of this Bouligand-type microstructure, as seen in Figure 3c. This thesis aims to build a better understanding of this unique collagen structure and mechanics and add to the recent research being done on the various aspects of the boxfish's dermal armor with the end goal of replicating its unique structure for novel engineering applications.

2 Background

2.1 General Information and Phylogeny of Boxfish

Boxfishes (superfamily Ostracioidea) belong to the Tetraodontiformes order, which includes pufferfish, triggerfish, trunkfish, and ocean sunfish, and have 37 species across the Aracnidae (deep water boxfishes) and Ostracidae (cowfishes and trunkfishes) families, as shown in Figure 7 [11]. Although several independent origins of body armor in fish have emerged, the boxfishes dermal armor proves to be one of the most unique. Among boxfish, the shape of their carapace differs from a square transverse section (e.g. *Ostracion*), to triangular (e.g. *Tetrosomus*) or oblong (e.g. *Anoplocapros*) [11]. In this work the *Lactoria cornuta* (longhorn cowfish) is analyzed and has a carapace shape most like the triangular-type.

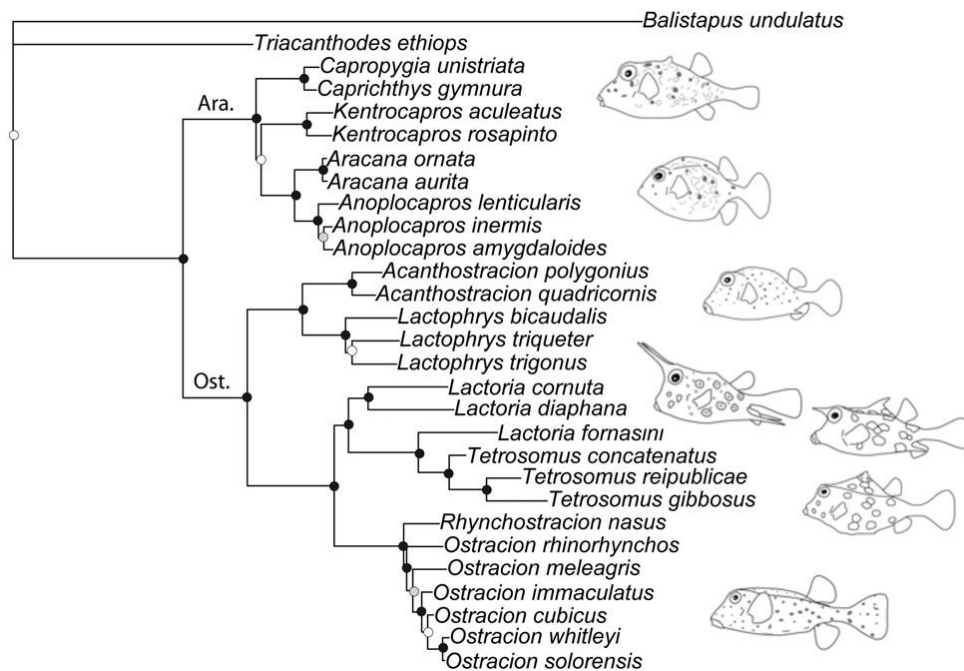


Figure 7. Maximum likelihood phylogenetic hypothesis of boxfish. Figure adapted from [11].

Aside from their unique armor, boxfish have also been studied for their ability to have surprising maneuverability despite having a shape that limits their undulation for enhanced speed

[12-17]. Boxfishes are surprisingly able to reach speeds greater than six body lengths per second, achieve a minimal turning radius, and have reliable control of their position. It has been shown that boxfishes are able to produce destabilizing vortices, seen in Figure 8, that promote enhanced maneuverability in highly turbulent waters [12,13]. It is postulated that this allows the boxfish to feed during harsh flow conditions and be able to efficiently navigate the coral reef habitat [12]. Therefore, when assessing the details of the boxfish's dermal armor for bioinspired applications we must highly consider both its role in movement and mechanical defense.

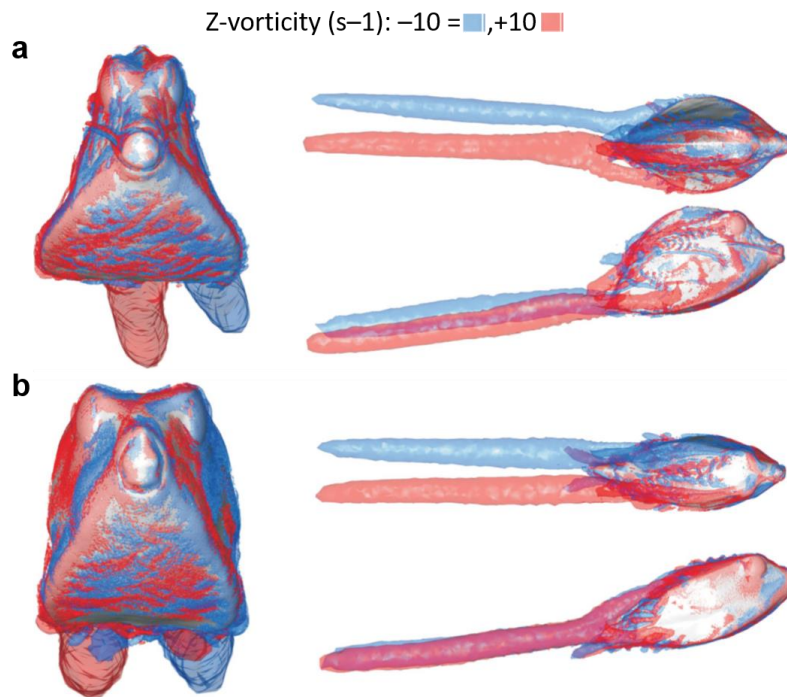


Figure 8. Vorticity patterns during 20° pitch angles of two differently shaped boxfish species: (a) *R. triqueter* and (b) *O. cubicus*. Each simulation shows frontal (left), dorsal (top right), and lateral (bottom right) views with +10 Hz (clockwise facing flow direction in red) and -10 Hz (anti-clockwise facing the flow direction in blue) iso-vorticity surfaces. Image adapted from [13].

2.2 Scute structure

Boxfishes are most notably characterized by their box-type carapace shape and their approximately hexagonal, non-overlapping scutes, as seen in Figure 9. When looked at under a microscope these hexagonal scutes are shown to have interdigitated, or sutured, interfaces as

seen in Figure 10e. This type of suture geometry is found in several other biological materials such as turtle shells (Figure 10b), mammalian skulls (Figure 10c), the pelvis of the threespine stickleback fish (Figure 10d), diatom frustules (Figure 10f), and armadillo osteoderms (Figure 10g) [18]. The sutured interfaces in these biological materials allow for localized control of flexibility and intrinsic strength of otherwise stiff materials [18].

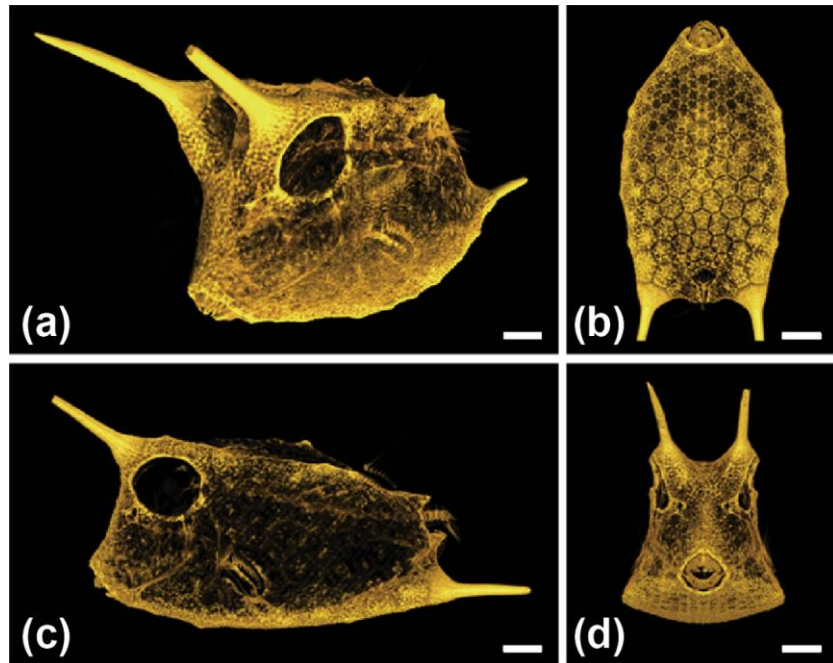


Figure 9. Micro-computed tomography images of the boxfish, *Lactoria cornuta*. (a) Perspective view; (b) Ventral view; (c) Sinister view; (d) Anterior view. Scale bars: (a–d) 5 mm. Figure adapted from [10].

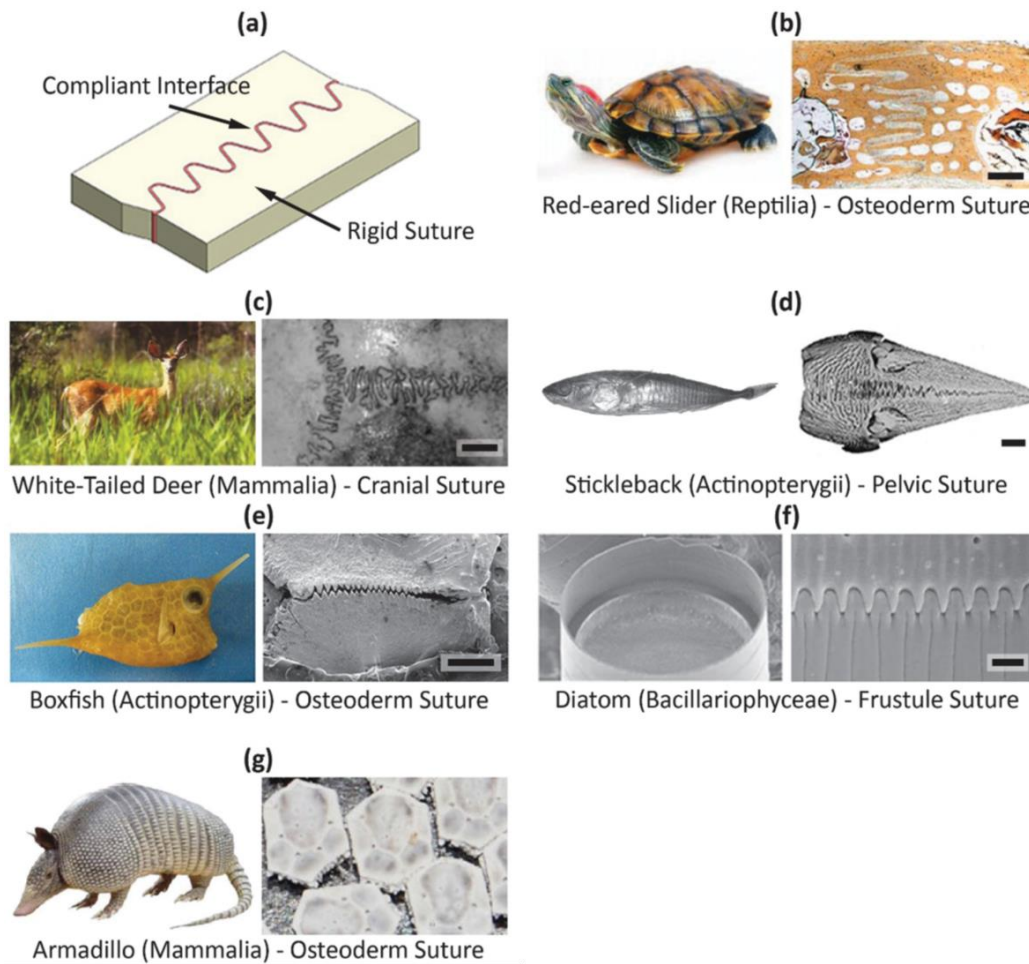


Figure 10. Various sutured interfaces found in biological materials. (a) Model of sutured interface with added compliant phase connecting both sides; (b) Red-eared slider with sutured osteoderms; (c) White-tailed Deer with cranial sutures; (d) Stickleback with pelvic suture; (e) Boxfish with scute sutures; (f) Diatom with frustule sutures; (g) Armadillo with osteoderm sutures. Scale bars: 1 mm, 1 cm, 1 mm, 500 μm , 1 μm for (b), (c), (d), (e), and (f), respectively. Figure adapted from [18].

Sutured interfaces have been explored by simulations, analytical modelling, and 3D printing experimentation by various researchers in the recent past [19-23]. Various aspects of sutured interfaces have been explored, including degree of interdigitation, different tooth geometries (e.g triangular, trapezoidal, and rectangular) with varying pitches among them, the ratio of moduli between the compliant and mineralized phase, and the addition of hierarchical or fractal-like sutures. However, most of this research assumes there is a compliant phase, as shown in Figure 10a, that bonds to the both sides of the sutured interface. The boxfish proves to be

unique in that its sutured interfaces lack this connective compliant phase, also known as Sharpey's fibers for collagenous interfaces [10]. Additionally, the boxfish proves to be unique in its wavelength and angle of its scute 'teeth' compared to the other animals shown in Figure 10 [10]. A mathematical model from Li et al. [23] determined that the strength-optimized angle in a triangular suture made of bone and collagen is $2\theta = 24^\circ$, which is similar to the other animals in Figure 10 but far from the boxfish's value of 50.6° [10]. Both the absence of Sharpey's fibers and its unique geometry of sutured interfaces demonstrate the boxfish is optimizing its dermal armor for other functions than strength and, therefore, warrants further research to better understand this unique biological composite.

Besseau and Bouligand [4] revealed the internal structure of the boxfish's scute and showed that there is both an outer mineral plate as well as a lower mineral plate that are connected by vertical mineral walls, as shown in Figure 11.

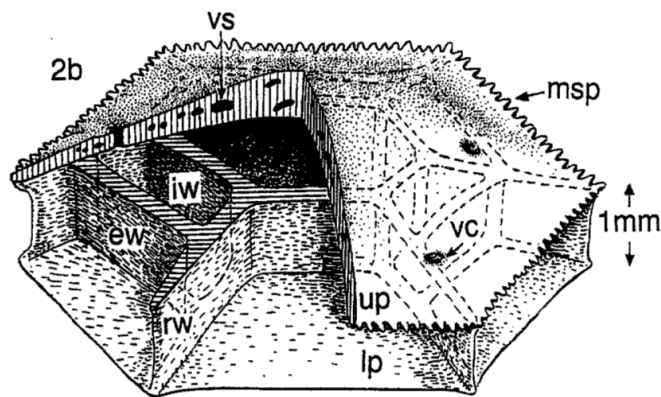


Figure 11. Schematic of mineralized plates and walls that make up a boxfish scute. The upper convex plate is bound to the lower concave plate with vertical walls. Although the majority walls follow the polygonal pattern of the scute, it is typical for a wall in one of these faces to be absent. In this study, they analyzed three species of *Ostraciidae* (*Ostracion lentiginosum*, *Ostracion tuberculatus*, and *Tetrasomus concatenatus*) that all demonstrated this structure. Figure adapted from [4].

In their study, three species of *Ostraciidae* (*Ostracion lentiginosum*, *Ostracion tuberculatus*, and *Tetrasomus concatenatus*) were analyzed and all revealed this similar mineral structure within their scutes. It was thought that this structure was representative of all boxfish, however recent research from Yang et al. [10] found that another species of boxfish (*Lactoria cornuta*) only possess the top mineral plate and do not have either a lower plate or vertical walls spanning the collagen base. However, the collagen's hierarchical organization, as will be discussed in the next section, remained similar despite this significant difference in their mineralized structures.

Although no research has been done to mimic this particular sandwich-style mineral structure seen in some boxfish, there are synthetic sandwich composites, as shown in Figure 12, that closely resemble this structure with the hexagonal honeycomb style (Figure 12a) appearing the most similar.

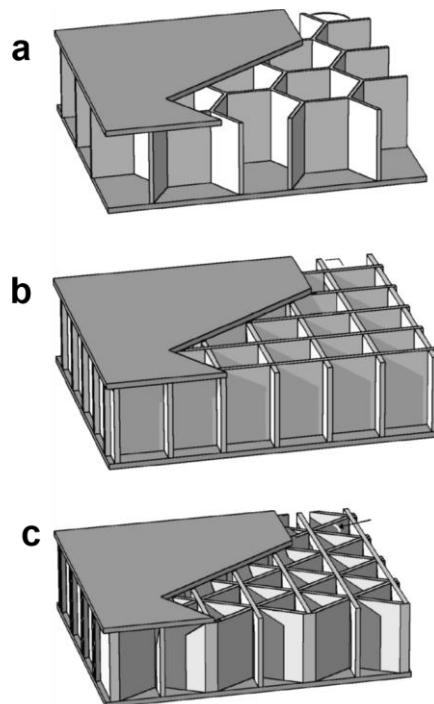


Figure 12. Three types of honeycomb sandwich structures: (a) hexagonal honeycomb, (b) square honeycomb and (c) triangular honeycomb. Figure adapted from [24].

Honeycomb sandwich composites are used in the wings of aircraft due to their optimization on the ratio of bending stiffness to density and usually consist of thin, stiff, and strong materials and a lightweight, compliant core like that of the boxfish [25]. This similarity may suggest the dermal armor of the boxfish, as compared to other natural dermal armors, is well-suited against bending caused from predator attacks. Although more research is necessary, the absence of a bottom mineral plate and the mineral walls in the *Lactoria cornuta*'s scute structure may suggest this structure has managed to achieve a similar resistance to bending without the costly need for more mineralized mass (i.e. the bottom plate and walls).

Recent studies have been applying bio-inspired designs into sandwich structures with promising results [26, 27]. By first researching and understanding how woodpeckers are able to sustain a multitude of high-impacts without sustaining brain damage, researchers learned how the use of the hyoid layer mitigates stress waves from the inner brain. Utilizing this understanding has allowed researcher to develop bio-inspired sandwich structures (Figure 13a-b) that have demonstrated an increase in 2.7 - 5.7 times higher impact resistance efficiency indices compared to more traditional structures. Furthermore, a similar bio-inspired sandwich structure was developed by utilizing the bi-directionally sinusoidal chitin structure found in the dactyl club of the mantis shrimp (Figure 13c-d) and demonstrated increased energy absorption capacity. Similarly, by further understanding the structure of the boxfish, as done in this thesis, we can begin to apply any novel findings to synthesize the next generation of impact resistant materials, such as novel sandwich structures.

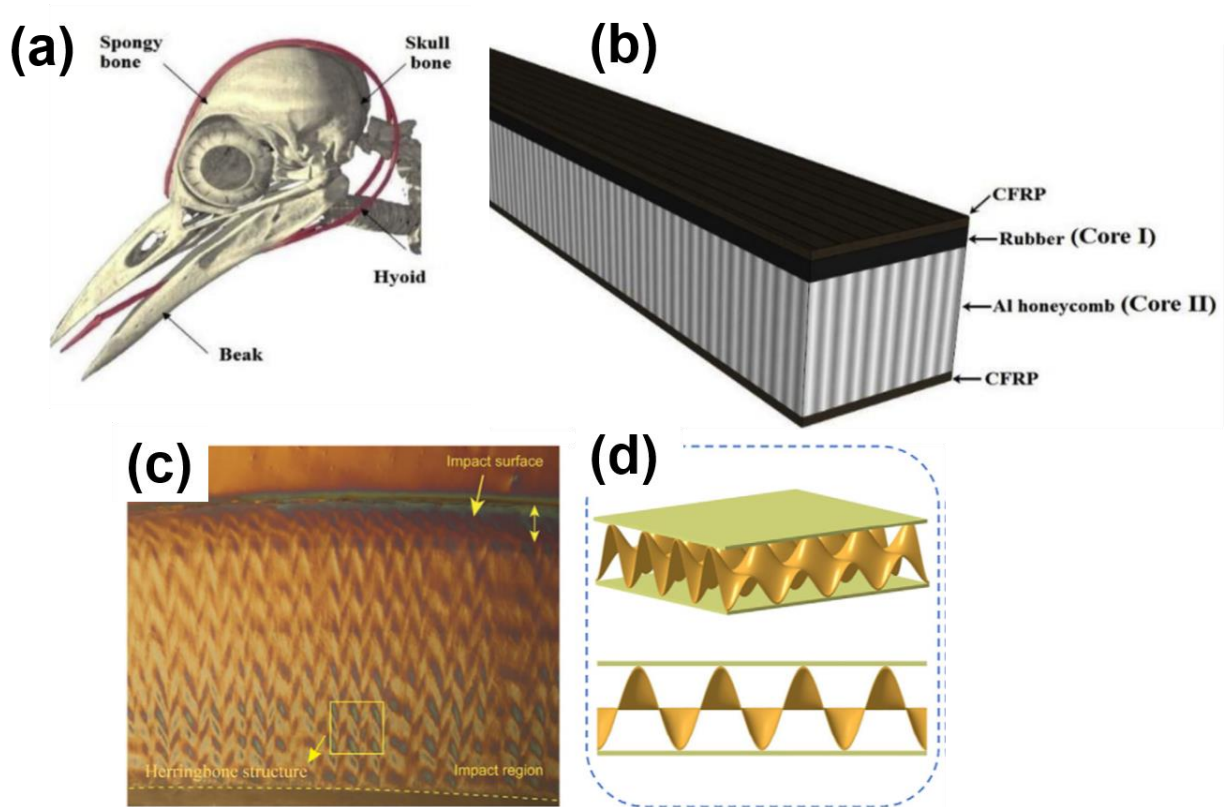


Figure 13. (a) Skull of woodpecker with highlighted hyoid layer which is responsible for mitigating stress wave around the skull to protect the brain; (b) Bio-inspired honeycomb sandwich structure that includes an additional core layer of rubber that acts similarly to the hyoid layer in the woodpecker skull; (c) Cross-sectional CT-scan of the dactyl club of a mantis shrimp; (d) Schematic representation of a bio-inspired sandwich structure that uses the bi-directionally sinusoidal structure found in the mantis shrimp dactyl club. Figure adapted from [26, 27].

2.3 Collagen Structure

2.3.1 Hierarchical Structure of Collagen Fibrils

Collagen is an essential biomaterial that serves as the basis for many biological composites (e.g. tendon and bone). It proves to be extremely versatile in creating materials of various material and mechanical properties. Collagen is commonly interfaced with hydroxyapatite (bone mineral) to create composites for various utility in animals. Figure 14 is an Ashby plot of the composite materials made from the natural synthesis of collagen and

hydroxyapatite materials and reveals how nature can fine tune the material properties (e.g. stiffness and toughness) to synthesize the evolutionarily advantageous composite that is needed.

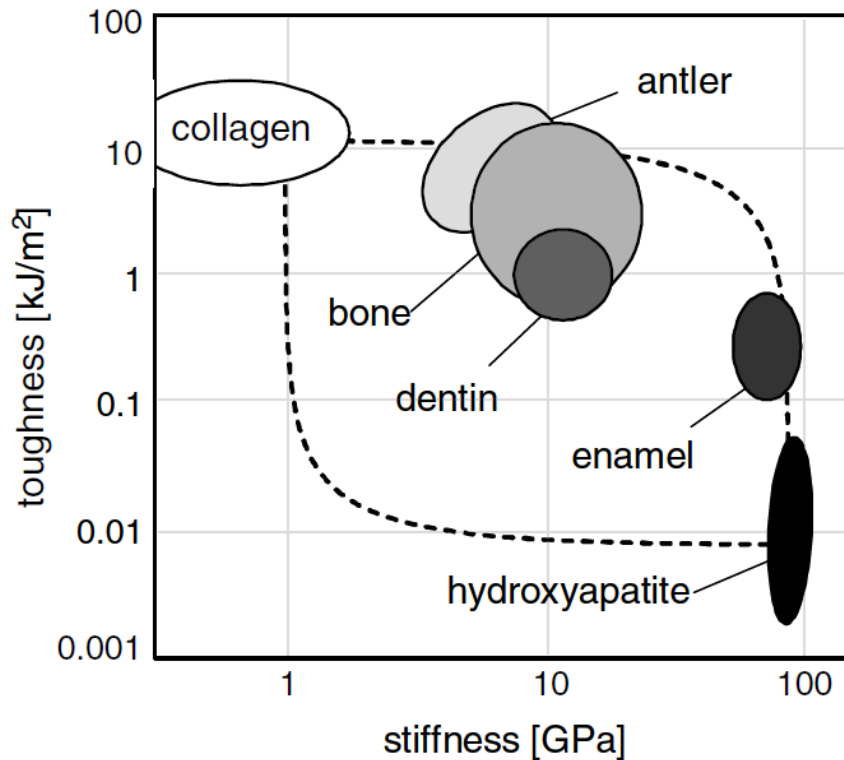


Figure 14. Ashby plot revealing the differences in toughness (fracture energy) and stiffness (Young’s modulus) among biomaterials made from collagen and hydroxyapatite. Figure adapted from [28].

Collagen alone is a complex hierarchical material and exhibits characteristic patterns that make it easier for researchers to confidently analyze them (e.g. with electron microscopy or small-angle X-ray scattering). Collagen’s first step in synthesis (Figure 15a) is in the form of a procollagen triple helix molecule made of amino acids (typically glycine, proline, and hydroxyproline). Cleavage of the ends of the triple helix molecule occurs (Figure 15b) and allows for the parallel self-assembly (Figure 15c) of these cleaved molecules to form a collagen fibril (Figure 15d) [29]. Due to the off-set molecules of the self-assembly, a characteristic period emerges (d-period, ~ 67 nm) from the gaps that periodically occur after every fifth molecule stacked. This d-period is a signature of the collagen fibrils and is used to study collagenous

materials in more depth (analogous to characteristic periodicities in crystal structures), as will be discussed in the next section.

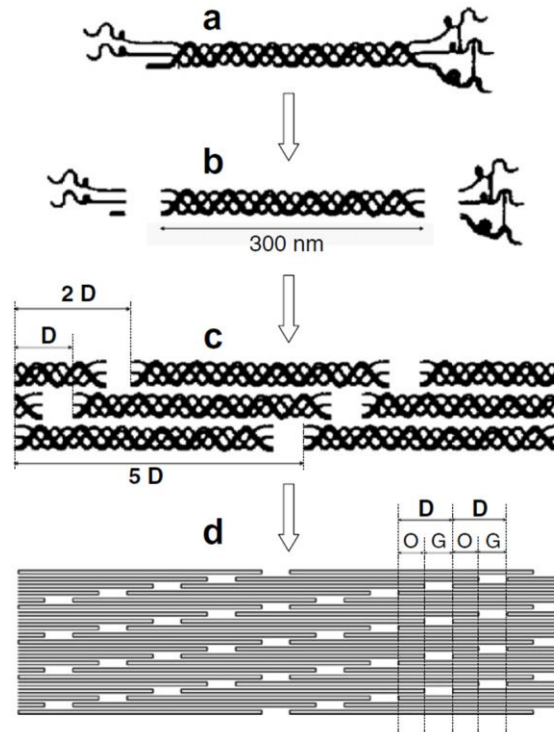


Figure 15. Hierarchical assembly of collagen fibrils. (a) Initial stage of procollagen molecule; (b) Cleavage of the propeptide ends; (c) Self-assembly of collagen molecules resulting in a staggering period, D (~ 67 nm); (d) Resultant collagen fibril with variations in density due to the overlapping of molecules. O is where there are no gaps and G is the gap region that occurs on one out of five stacked collagen molecules. Figure adapted from [29].

Collagen fibrils are not the end of the hierarchy; collagen fibrils form other biological materials by undergoing varying degrees of mineralization with hydroxyapatite crystals. For example, bone (Figure 16) is made up of highly mineralized collagen fibrils embedded in an extrafibrillar matrix [30]. Due to bone’s complex structure, it can manage stress through multiple mechanisms giving yield to the impressive balance of strength and toughness that is rarely seen in synthetic composites. Gupta et al. [30] used a combination of *in-situ* tensile testing to gather overall tissue strain and small-angle X-ray scattering to track the d-period of collagen during deformation to obtain a fibril strain. By combining these techniques, researchers are able to

bridge the gap between overall composite response and the nanoscale mechanisms responsible for the response thereof.

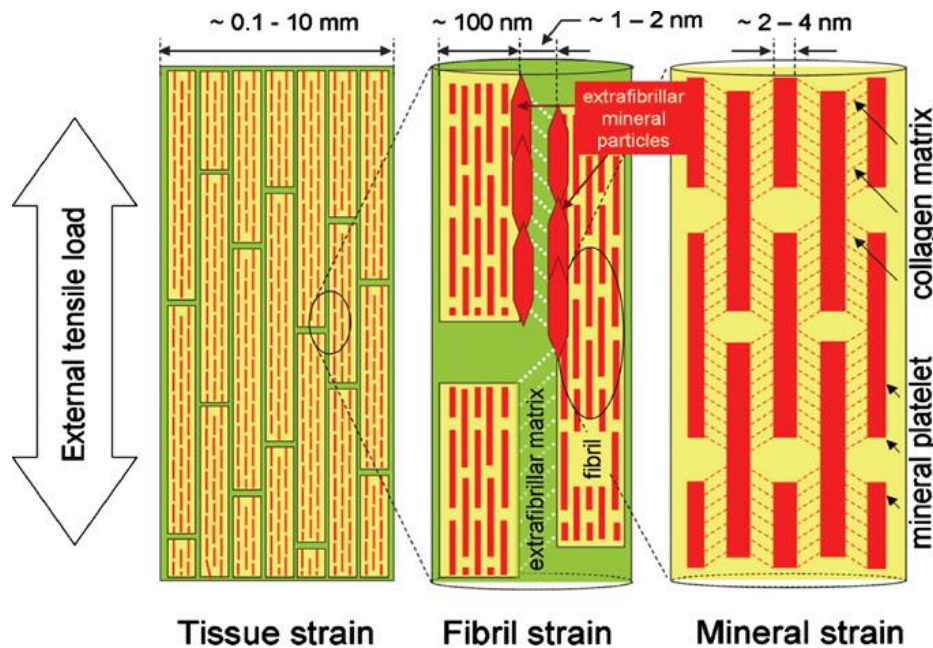


Figure 16. Hierarchical assembly of bone and its deformation response to tensile load at the tissue level, fibril array level, and mineralized collagen fibrils. The mineralized fibrils (*Center*) transfer the stress from tension by shearing of the thin layers of extrafibrillar matrix (white dotted lines showing direction of shear). Each mineralized fibril (*Right*) the platelets deform and transfer the stress from tension by shearing the interparticle collagen matrix. Figure adapted from [30].

2.3.2 Small Angle X-ray Scattering

As technology continues to develop, the study of collagen and other biomaterials is growing rapidly. Examples of these technologies include small angle X-ray scattering (SAXS), ultra-small angle X-ray scattering, and small-angle neutron scattering. These technologies use similar methods to the more widely known X-ray and neutron diffraction techniques but aim to analyze periodicities at larger length scales which enable these diffraction techniques to be used on polymer or multi-molecular systems. Furthermore, *in-situ* SAXS is also being utilized to study the mechanics of hierarchical biomaterials, where mechanical testing is performed simultaneously with SAXS analysis under various controlled environmental conditions [31, 32].

Examples of studies using these technologies include: carbon fiber composites, ceramic matrix composites, flexible macromolecules in solution, fracture resistance of human cortical bone, mechanical behavior of femoral cortical bone in osteoporotic individuals, buckling in bone nanostructure during mechanical testing, structural effects on the healing of human cornea, twisted plywood collagen structure of teleost scales, and the mechanical adaptability of Bouligand-type structures [31-38].

Of key interest in this thesis is *in-situ* SAXS, which is used to determine the preferential directions of alignment in collagen fibrils in the boxfish's dermal armor and how they behave under loading. Recently, Zimmermann et al. [2] has utilized *in-situ* SAXS to both observe the Bouligand-type structure in the collagen in the scales of the *Arapaima gigas*. The collagen's d-period (~60 nm) and fibril spacing (~50 nm) periodicities, mentioned in the previous section, are correlated with the diffraction patterns produced by the SAXS analyses (Figure 17) which are then tracked during mechanical loading (Figure 18). This study is a key example of how *in-situ* SAXS can be utilized to understand the structure and mechanics of biological materials with impressive capabilities such as the dermal armor of the *Arapaima gigas* or boxfish.

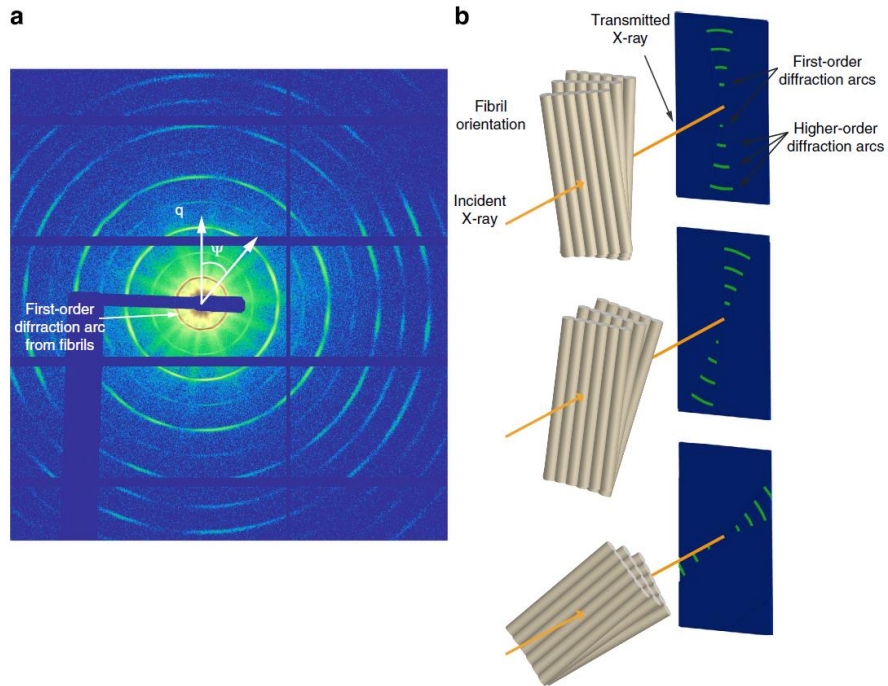


Figure 17. Small-angle X-ray scattering (SAXS) diffraction pattern from *Arapaima gigas* scales. **(a)** The overall diffraction pattern from the periodicity in the collagen fibrils of the scale; **(b)** Each alignment of collagen fibrils results in arcs in the diffraction pattern that are parallel to the d-period of the collagen fibrils. The Bouligand-type structure in the scale is represented by the several distinct arcs that rotate around completely. Coordinates used are the radial direction, q , and the angle, ψ . Figure adapted from [2].

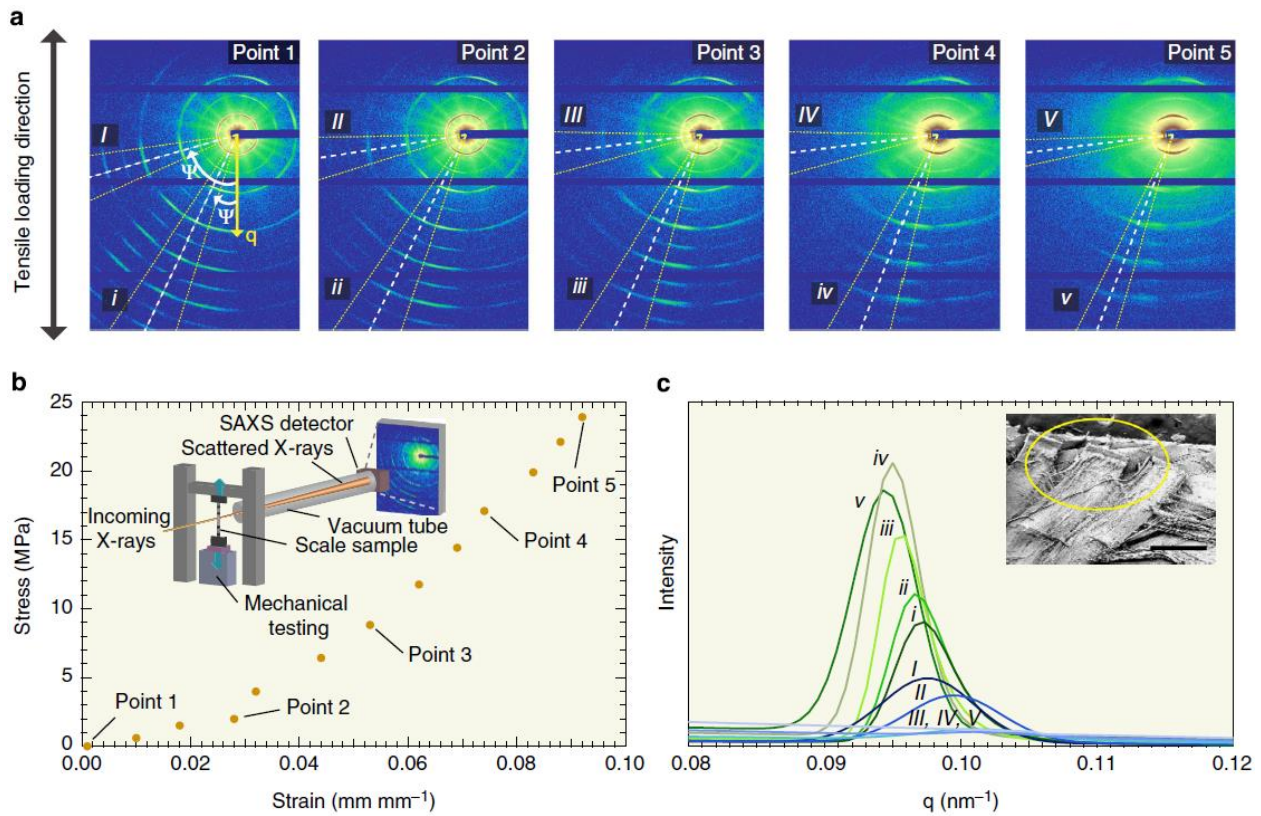


Figure 18. *In-situ* small-angle X-ray scattering (SAXS) analysis on *A. gigas* scale collagen structure. (a) Five snapshots of the SAXS diffraction pattern during tensile mechanical loading of a scale. Several fibril orientations are seen, but two nearly orthogonal orientations are considered. One orientation is nearly perpendicular to loading axis, while the other is nearly parallel. (b) Stress-strain curve of tensile loading which corresponds to the points taken in (a) with inset image showing experimental set-up. (c) The diffraction patterns were converted to 1D intensity versus q through integrating intensity arc length for arcs (i-v) and (I-V) for the first order peaks. The fibrils represented by arcs (i-v) begin to align with the tensile axis which is shown by an increase in intensity and exhibit tensile strain which is shown by a decrease in q . Conversely, the fibrils represented by arcs (I-V) have a positive shift in q with loading which indicates compressive strain and at higher loading the peaks disappear which suggest interfibrillar separation. Figure adapted from [2].

2.3.3 The Bouligand-type Structure

Bouligand and Besseau first analyzed the complex collagen structure seen in the boxfish [4]. They discovered the unique mineral structure, as mentioned in the previous section, as well as the different collagen arrangements using optical microscopy with polarized light and

transmission electron microscopy. It was found that the boxfish exhibited a similar collagen structure that has been previously observed under histological examination with other armored animals (e.g. crabs and tortoises). They described this reoccurring structure as a twisted plywood structure because plywood contains superimposed layers of aligned fibrils with a 90° shift between each layer, as shown in Figure 19a. Moreover, the twisted plywood structure, now referred to as the Bouligand structure, has a smaller and constant angle shift between each layer, as shown in Figure 19b. This geometry appears to take on characteristic arcs when viewed through an oblique cross-section.

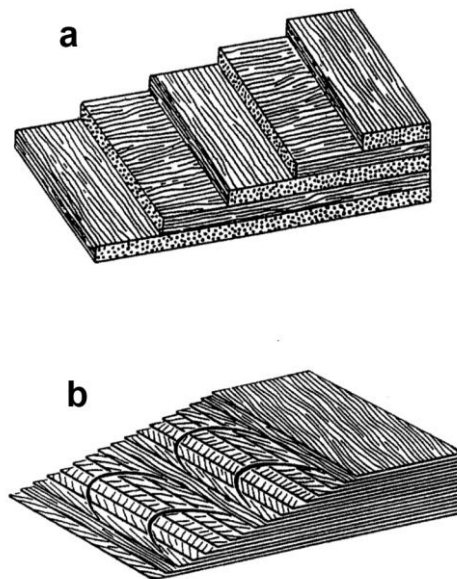


Figure 19. (a) Plywood structure with 90° rotation of fibrils in each layer. (b) Twisted plywood structure with a small angle rotation between each equidistant layer. When observed through an oblique slice the structure reveals its characteristic arcs. Figure adapted from [4].

Research on biological materials continues to find different animals with a Bouligand-type structure. Example of these animals include various insects (e.g. beetles, Figure 20a) [5,39], various crustaceans (e.g. mantis shrimp, Figure 20b) [3,40,41], various fish (e.g. coelacanth,

Figure 20c) [2,42,43], and human bone [44]. Although these animals all share a similar Bouligand-type structure, they still vary significantly in other aspects. For example, different types of constituent fibers are found that make up this structure (e.g. mineralized collagen for the coelacanth and chitin in *Cotinis mutabilis* beetle) and different pitch sizes by orders of magnitude are found (e.g. pitch size in *C. mutabilis* is ~220 nm while pitch size in *Odontodactylus scyllarus* mantis shrimp is ~100 μm). However, what all these biological materials do have in common are tough, ductile, and lightweight protective layers due to the Bouligand-type arrangements of their respective fibrous constituents.

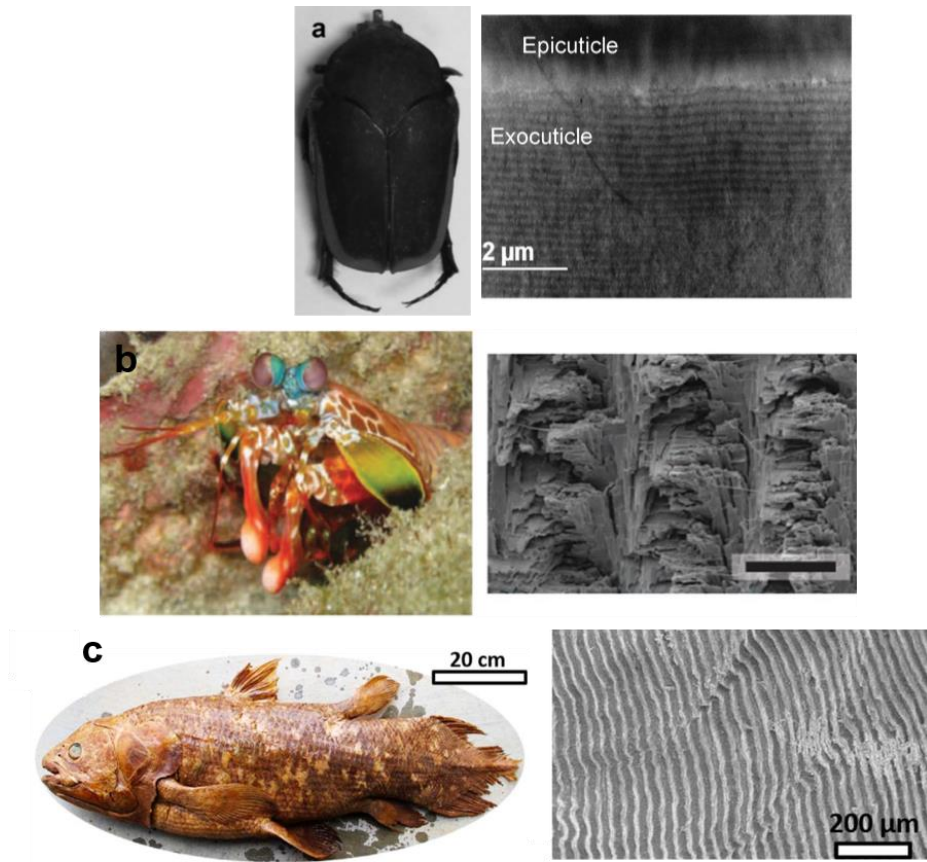


Figure 20. Examples of animals that contain Bouligand-type structures: **(a)** The exocuticle region of the *Cotinis mutabilis* beetle shows a Bouligand-type structure made of chitin fibers in proteinaceous matrix with a pitch size of ~ 220 nm; **(b)** The dactyl club's periodic region of the *Odontodactylus scyllarus*, or mantis shrimp, contains Bouligand-type structure made of mineralized chitin fibers and a pitch size of ~ 100 μm (scale bar, 75 μm). **(c)** Coelacanth (*Latimeria chlaumnae*) with the double-twisted Bouligand-type structure made of mineralized collagen fibers. It is noted that the Bouligand-type structure's pitch can vary by several orders of magnitude. Figure adapted from [5,41,42].

The most recent work published on the collagen structure of the boxfish by Yang et al. [10] have claimed that there is not a Bouligand-type structure, but rather a ladder-like structure as shown in Figure 21. The high magnification of the collagen surface revealed perpendicular interfaces which gave good reason for the authors to hypothesize that the Bouligand structure is not present, but rather a new proposed ladder-like structure where columns of unidirectional fibers are connected through perpendicular collagen planes. This thesis attempts to confirm that

there is a Bouligand-type structure by applying more structural characterization techniques (i.e. micro-computed tomography, *in-situ* scanning electron microscopy, *in-situ* small angle x-ray scattering, and nanoindentation).

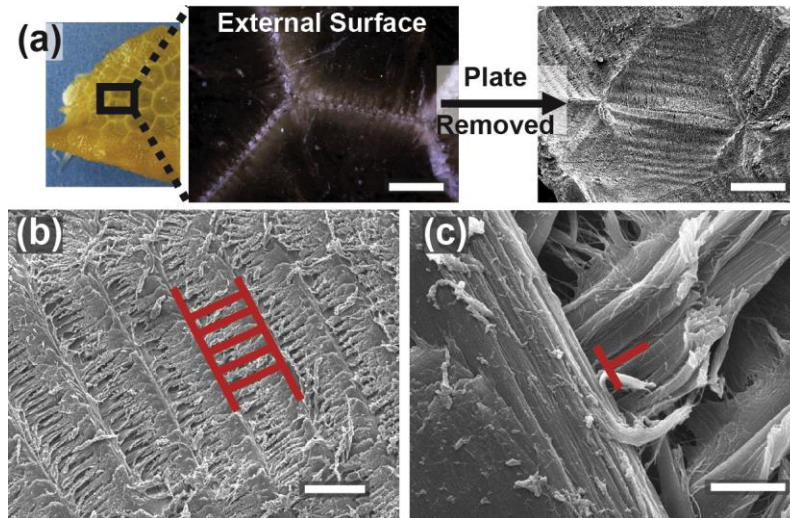


Figure 21. (a) Top view of mineralized surface of boxfish (*Lactoria cornuta*); (b), (c) Scanning electron microscopy of top view with mineral plate removed revealing an apparent ladder-like structure. Scale bars: (a) 500 μm ; (b) 100 μm ; (c) 5 μm . Figure taken from [10].

Many Bouligand-type structures in biological materials consist of off-set planes of parallel biopolymer fibers, but the interfibrillar gaps seen in the lobster *Homarus americanus* demonstrates a unique archetype of the Bouligand-type structure. Figure 22, adapted from Romano et al. [45], reveals a cross section of the Bouligand-type structure seen in the lobster. It is proposed that these interfibrillar gaps allow for the transportation of ions for mineralization processes and provide a high density of interfaces to resist fiber pullout [45, 46]. A similar structure appears in the boxfish's collagen, that is seen by optical microscopy done by Besseau and Bouligand [4], shown in Figure 23. Arcs can be seen which may be cross-sections of a similar Bouligand-type structure which consists of an array of interfibrillar gaps.

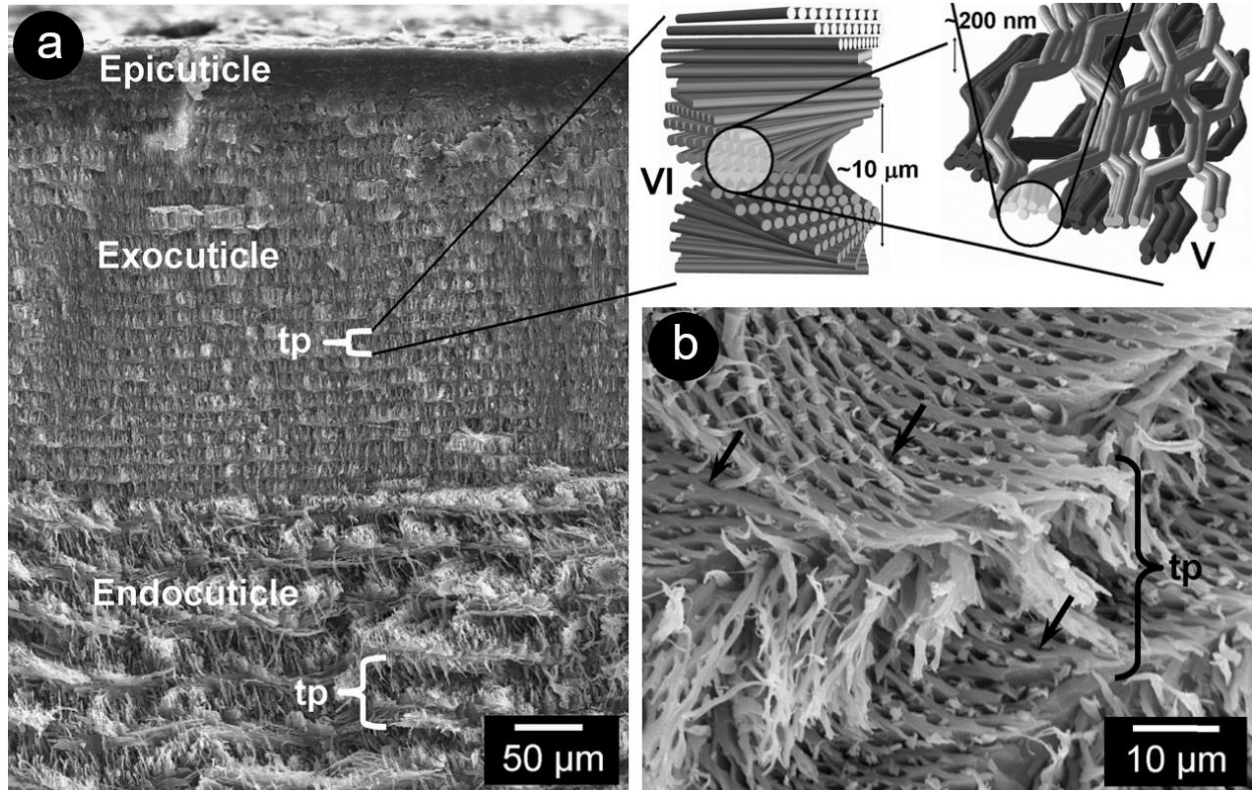


Figure 22. (a) Scanning electron microscope (SEM) image of the cross-section of the exoskeleton of the cuticle in a lobster *Homarus americanus*. Schematic representations are given of the twisted plywood (Bouligand-type) structure with the helical interfibrillar gaps within the twisted plywood structure; (b) SEM of oblique cross section of lobster revealing the network of helical gaps (shown by arrows). Figure adapted from [44].

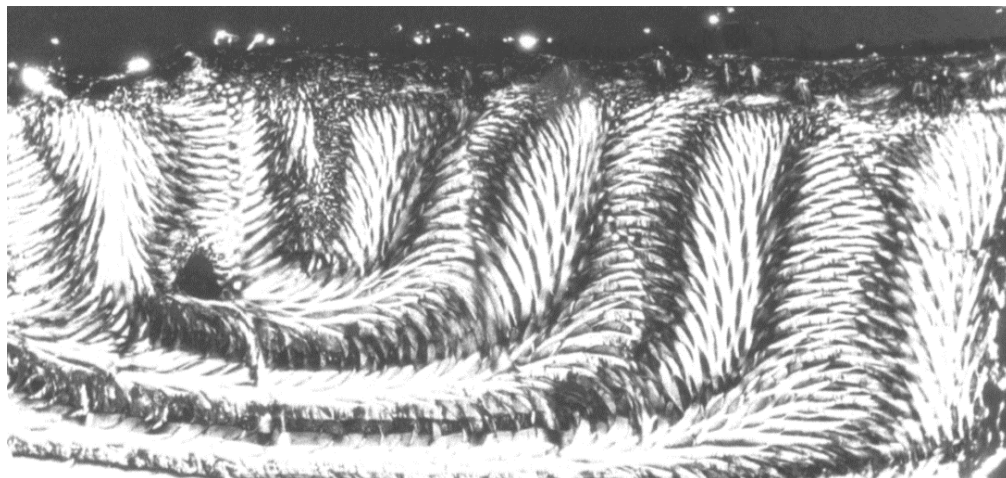


Figure 23. Transverse section of boxfish scute using optical microscopy between crossed polar. Figure adapted from [4].

2.3.4 The Nested-bowl Structure

Among the different types of Bouligand structures previously mentioned, the Boxfish seems to be among the most unique due to an additional hierarchy of organization, referred to here as the nested-bowl structure as shown in Figure 24. The bottom region, where the helical axis is parallel to the thickness of the scute, becomes tapered with each subsequent layer approaching upward to the outer surface. Similarly, the side regions become tapered laterally as their layers approach the center. This gives rise to a structure that appears as if bowls are nested within another. The reason for this unique architecture remains for the most part unknown, although further bioinspired and biomimetic experimentation and simulation could yield valuable results as has been done with the simplified Bouligand structure. [27,30-33]

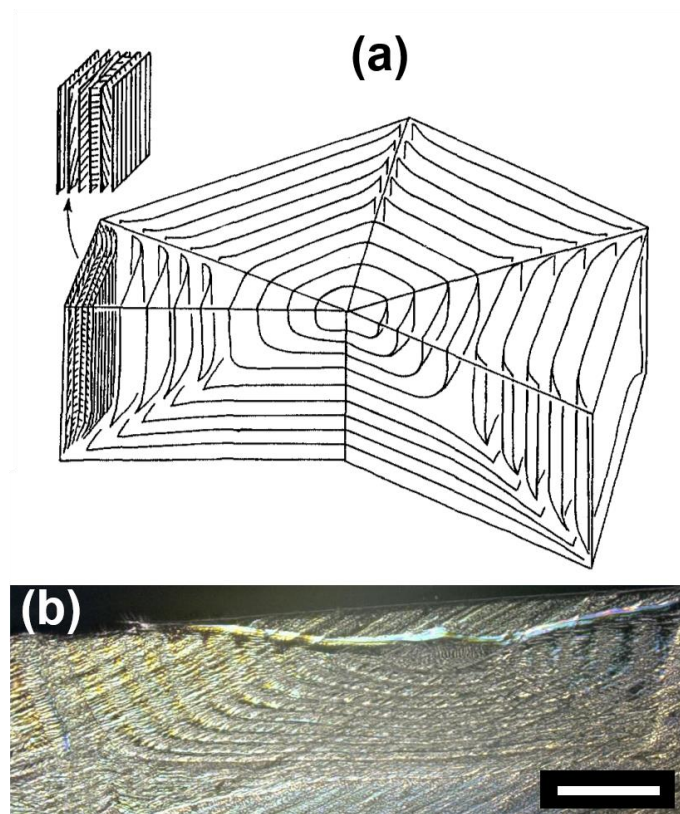


Figure 24. The nested-bowl structure found in the scute of the boxfish. **(a)** Simplified schematic of collagen structure in boxfish scute; **(b)** Confocal microscope image of cross-section of boxfish scute revealing the nested-bowl structure (scale bar, 500 μm). **(a)** adapted from [4]

2.4 Mechanical Characterization

Recent research done by Yang et al. [10] used various experimental techniques to characterize and quantify the mechanical properties of the boxfish (*Lactoria cornuta*). Scute interfaces were tested in tension (Figure 25), in shear (Figure 26), and with a hexagonal penetration test (Figure 27) to remove a single scute. Their results showed that the scute interface was three times larger in strength and six times larger in stiffness during tension than in shear.

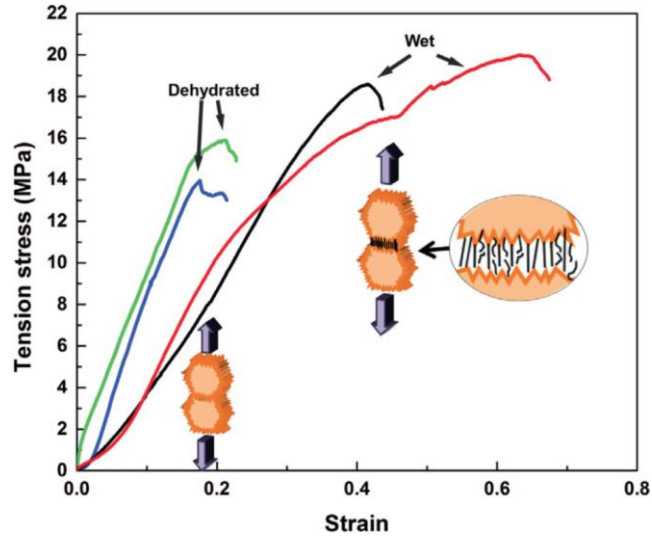


Figure 25. Tensile stress-strain results of two connected boxfish (*Lactoria cornuta*) scutes. Both wet and dehydrated samples were tested with the wet samples exhibiting a lower elastic modulus. Figure adapted from [10].

Moreover, in the tension and penetration tests, failure occurred predominantly in collagen fibers at the interface between scutes. During shear testing, the triangular teeth at the sutured interfaces interlocked and further led to tooth fracture. Overall, they concluded that the collagen fibers at the interfaces are weaker than the collagen within the nested-bowl structure and cause failure to occur predominantly in these interfacial regions.

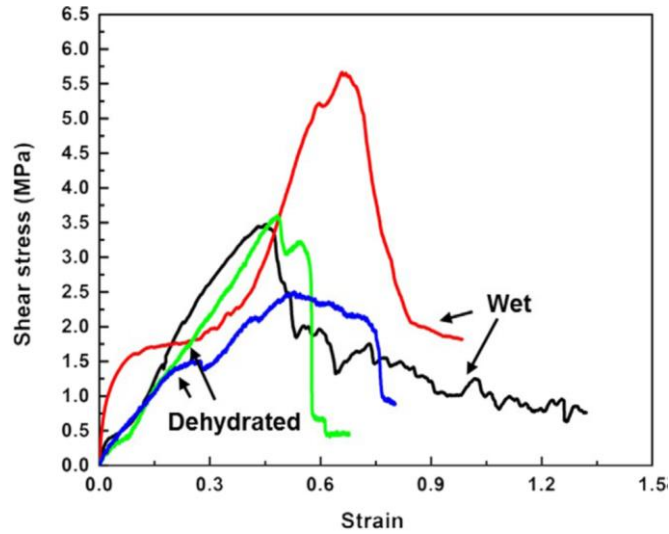


Figure 26. Shear stress-shear strain results of two connected boxfish (*Lactoria cornuta*) scutes. Both wet and dehydrated samples were tested. Large variance in data due to different samples having significant differences in the number of teeth interlocking and subsequently failing. Figure adapted from [10].

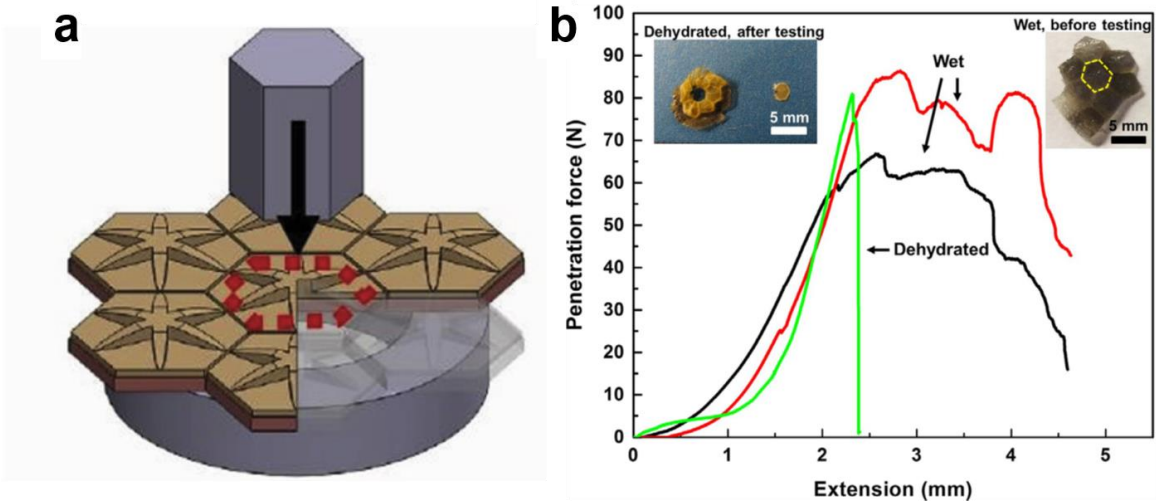


Figure 27. (a) Schematic of the punch test experiment with array of boxfish scutes; (b) Penetration test results on boxfish (*Lactoria cornuta*) scutes. Both wet and dehydrated samples were tested with the wet samples having a gradual failure process due to the lubrication between collagen fibers. Figure adapted from [10].

3 Hypothesis

This thesis aims to characterize the structure and mechanical properties of the carapace of a species of boxfish, *Lactoria cornuta*. The boxfish carapace sacrifices flexibility and mobility in return for an efficient mechanical defense against larger predators. Previous studies have made contradicting statements with regards to whether the collagen structure within the boxfish scute is of a Bouligand-type [4,10]. Therefore, the main hypotheses addressed in this thesis are:

- (I) The mechanical properties of this dermal armor are allowing the boxfish to efficiently defend against its predators.
- (II) The collagen structure within a boxfish scute is a Bouligand-type.

4 Materials and Methods

Three boxfish samples were obtained from the Scripps Institution of Oceanography at the University of California, San Diego (*Lactoria cornuta*, catalog numbers SIO 14-20, SIO 95-125, SIO 95-141). Samples were preserved in a 1:1 isopropanol and water solution to induce a semi-dehydrated state. Two samples measured ~50 mm in length and one measured ~100 mm in length. For most experiments mentioned in this section the surface plate was carefully polished off using high grit sandpaper, then sonicated to remove any contamination.

4.1 Confocal Microscopy

Confocal microscope image was taken using a Keyence VHX1100. Samples were carefully polished to remove the top mineral plate and further infiltrated with OsO₄ and fixed into epoxy to enhance imaging contrast (Appendix A).

4.2 Micro-Computed Tomography

Micro-computed tomography (μ -CT) was performed using a Zeiss Versa 510 microscope with a voxel size of 535 nm. The same samples used for confocal microscopy were used for μ -CT and, therefore, had the mineral plate carefully removed and enhanced contrast from OsO₄ staining (Appendix A). μ -CT images (2,401 projections) were edited and stitched together using the Amira software by Thermo Fisher Scientific to create a high-resolution 3-dimensional image.

4.3 Nanoindentation

Nanoindentation was performed in collaboration with the Kisailus Biomimetics & Nanostructured Materials Lab at the University of California, Riverside. Nanoindentation was performed at room temperature using a TI 950 TriboIndenter (Hysitron, USA) (Figure 28) with a

fluid cell Berkovich probe and a trapezoidal load function with five seconds for each the loading, hold, and unloading. The indents, totaling at 2,501 indents, were displacement controlled to 2 μm depth and 10 μm spacing between each indent in both horizontal and vertical axes, respectively. A preload of 15 μN was used to ensure that the tip found the sample surface. Nanoindentation was performed on a boxfish scute with the mineral plate carefully polished off and soaked in Hank's Balanced Salt Solution before and consistently topped off during the process, as shown in Figure 28.

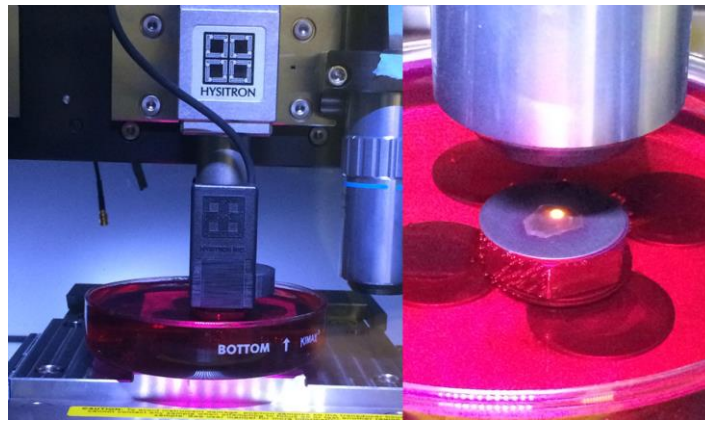


Figure 28. Hydrated nanoindentation was performed using a TI 950 TriboIndenter (Hysitron, USA) on the top side of a boxfish scute with its mineral plate carefully removed from polishing.

4.3.1 Nanoindentation Data Analysis

Nanoindentation data were processed to obtain the reduced modulus E and hardness H using the Oliver-Pharr method, as detailed in this section (Figure 29) [48].

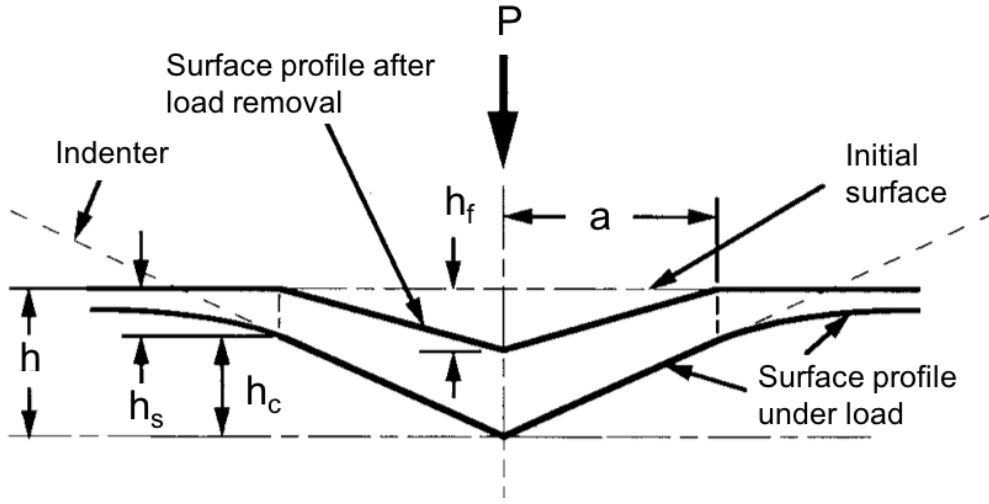


Figure 29. Generalized schematic of a nanoindentation procedure. The load P , radius of contact circle a , the final depth of the residual hardness impression h_f , contact depth h_c , total displacement of sample h , the displacement of the surface at the perimeter of contact h_s . Figure adapted from [48].

The reduced modulus E_r , which differs from the elastic modulus by accounting for the deformation of the indenter, is obtained from the following expression:

$$E_r = \frac{\sqrt{\pi}}{2} \frac{S}{\sqrt{A}} \quad (4.1)$$

where S is the slope during the first steps of unloading and A is the contact area which is a function of contact depth of the indenter. For a Berkovich tip, the projected area is calculated using:

$$A(h_c) = 24.5h_c^2 \quad (4.2)$$

Furthermore, hardness can be calculated using the expression:

$$H = \frac{P_{max}}{A} \quad (4.3)$$

where P_{max} is the peak load during indentation.

4.4 *In-situ* Scanning Electron Microscopy

In-situ Scanning Electron Microscopy (SEM) testing was performed using a Gatan Microtest 2kN bending stage (Gatan, Abington, UK) in a S-4300SE/N variable pressure scanning electron microscope (Hitachi America, Pleasanton, CA, USA). Five samples were tested with the mineralized plate intact and seven were tested with the mineralized plate removed. Prior to all testing, samples were rehydrated in hanks balanced salt solution (HBSS) for 24 hours, then immediately tested, to ensure that all tests were performed in a hydrated state. To understand the rigid, non-overlapping interfaces of the boxfish's armor, samples were tested in a SEM with tension and shearing loading modes (Figure 30) with a focus on the interface between scutes. To ensure this, samples for mechanical testing were carefully sectioned from the boxfish to include exactly two scutes with a single, unaltered interface between them.

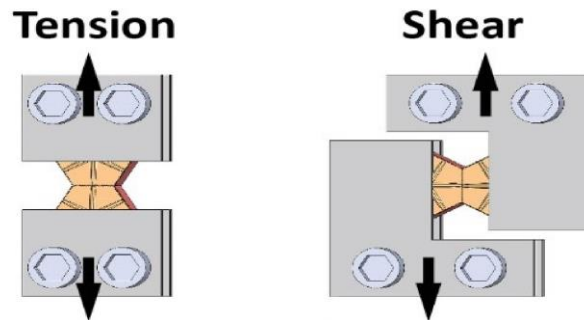


Figure 30. Experimental set-up of the *in-situ* scanning electron microscopy mechanical loading in both tension (left) and shear (right). Two neighboring scutes are held on opposing sides and imaged using SEM before and after deformation takes place. Experiments were done both with and without the mineral plate removed.

4.5 *In-situ* Small Angle X-ray Scattering

In-situ small angle x-ray scattering (SAXS) testing was performed at beamline 7.3.3 (Hexemer et al., Journal of Physics 2010) at the Advanced Light Source (Lawrence Berkeley

National Laboratory). We measured, at the nanoscale level, the deformation of collagen's fibril during *in-situ* tensile loading. This technique allows us to measure simultaneously the deformations at the collagen scale and at the tissue scale. Extremities of the boxfish scale were gripped between clamps. *In-situ* tensile and shear tests were performed inside the hutch (similar set-up to Figure 30) at a displacement rate of 5 $\mu\text{m/s}$ with a TST350 Tensile Testing Stage (Linkam Scientific Inc.). During the test, samples were exposed to x-ray beam of 10 keV energy for 1 s every 7.5 s. The cumulated irradiation dose was kept underneath the limit of 30 kGy to minimize the effects on mechanical behavior.

The collagen fibril's d-period (i.e. approximately 67 nm regular pattern of gap and overlap within the fibril) was measured from shifts in the Bragg peak positions as the sample is being loaded. Knowing the d-period at a specific load level and at zero load allows the deduction of the strain in the collagen fibril at this load level. After converting the 2D diffraction ring sectors to 1D data plots, the 1D datasets were fitted with a Gaussian function and a fourth-order polynomial to determine the collagen peak position with respect to the tensile axis. Moreover, tissue strains were obtained by measuring the change in spacing of dots and patterns on the sample's surface using digital image correlation software.

SAXS can provide microstructural data of relatively low-density materials, such as collagen. Previous reports on the use of SAXS on the collagen structures in fish scales have shown a diffraction pattern with distinct concentric arcs and dots, corresponding to the harmonics of the d-period of the collagen fibril and fibril spacing, respectively (Figure 31). [2,38].

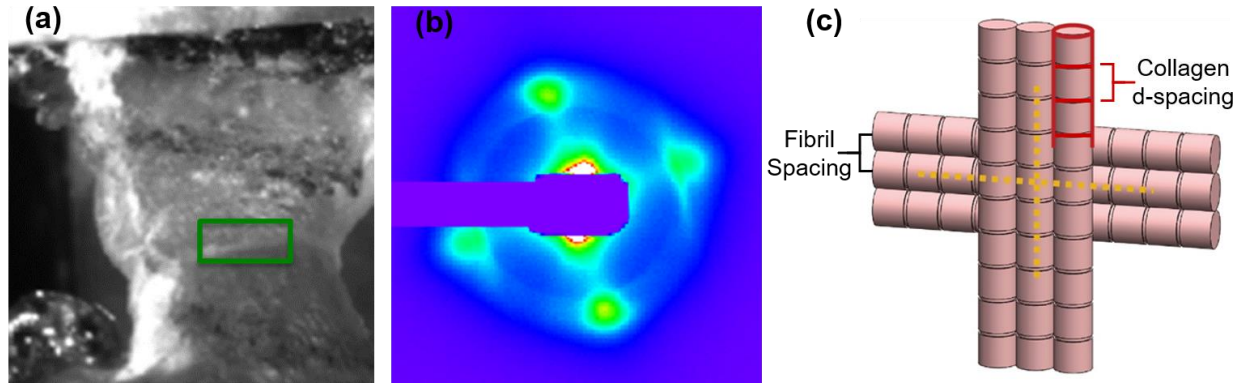


Figure 31. (a) Optical micrograph of two neighbored boxfish scutes anchored vertically to apply a tensile load. Green box represents approximate x-ray beam-size and location ($\sim 900 \mu\text{m}$ by $300 \mu\text{m}$); (b) Example of *in-situ* small angle x-ray scattering pattern from boxfish sample; (c) Schematic representation of interpreted collagen structure. A pair of arcs and a pair of dots, (a), represent the periodicity of the collagen d-spacing and collagen fibril spacing in a preferential direction. Two pairs are observed of each; therefore, two preferential directions are present in this representative sample.

5 Results and Discussion

5.1 Confocal Microscopy

Confocal microscopy images were taken to obtain a top-view (Figure 32) of the overall collagen structure inside a boxfish scute. Figure 32a reveals the periodic structure spiraling and conforming to the overall hexagonal shape of the scute. Figure 32b reveals the top side of a triple interface between three neighboring scutes. This region changes from a more textured structure within the scute to a darker and simplified structure at the interface. Moreover, the arcs viewed on the inner region of the scute, which are representative of the helical interfibrillar gaps within the bulk of the collagen (shown in the next section), are no longer seen in the interfacial region.

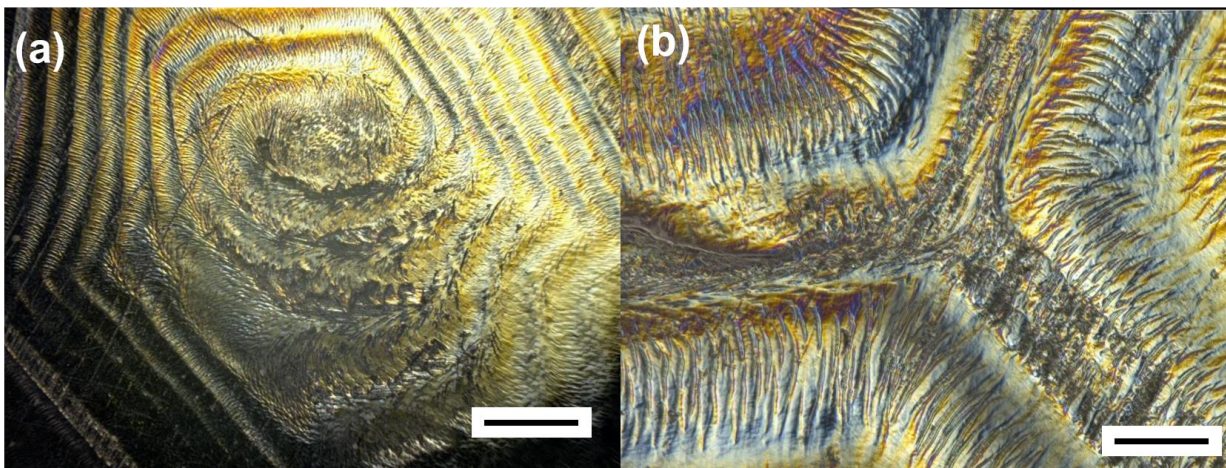


Figure 32. Confocal microscopy top view of the collagen in a boxfish scute. **(a)** After careful removal of mineral plate, the periodic collagen structure can be seen. Bottom portion of scute has been damaged through handling (Scale bar, 500 μm). **(b)** Zoom in on the triple interface of three scutes. The characteristic arcs of the Bouligand-type structure can no longer be observed in this interface (Scale bar, 100 μm).

Confocal microscopy images were also taken of the side-view of the collagen structure within a boxfish scute, as shown in Figure 33. Figure 33a reveals the cross-section of a single scute. A nested-bowl structure can be seen where the periodic axis is orthogonal and parallel

with respect to the thickness of the scute in the upper/side and bottom/middle areas, respectively. Figure 33a also reveals that the pitch length (180° rotation of collagen fibers) changes significantly between the upper/side (100 to 200 μm) and bottom/middle areas (~50 μm). This difference in pitch length may correlate with a difference in the density and stiffness of the two regions. Figure 33b is a cross-section of the interface between neighboring scutes. Similar to Figure 32b, it demonstrates that the interfacial collagen appears to have a different texture and is missing the characteristic arcs we see within the nested-bowl region.

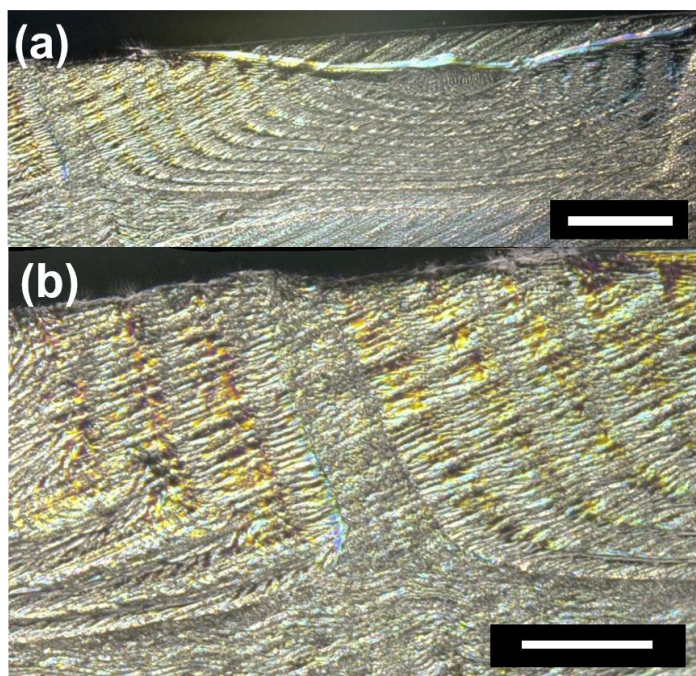


Figure 33. Confocal microscopy image of boxfish scute cross-section. **(a)** Cross-section of whole scute revealing the nested-bowl structure. The pitch length in the top/side regions (100 to 200 μm) is significantly larger than the bottom/middle regions (~50 μm). (scale bar, 500 μm); **(b)** Zoom in on the cross-section of the interface between adjacent scute. The lack of texture to the surface is indicative of a less structured region as compared to inside the scute (scale bar, 200 μm).

As common with oblique cross-sections of Bouligand-type structures, circular arcs are observed in the boxfish scute (Figure 34). The nested-bowl structure is shown in Figure 33a but not in Figure 31 because the angle of viewing with respect to the periodic axis of the collagen

structure changes from orthogonal (periodic axis is in-plane) to parallel (periodic axis is out-of-plane), respectively. Furthermore, the interfibrillar gaps seen in Figure 32 are shown to rotate from left to right creating the characteristic circular arcs seen in other Bouligand-type structures because the cross-section is slightly oblique.

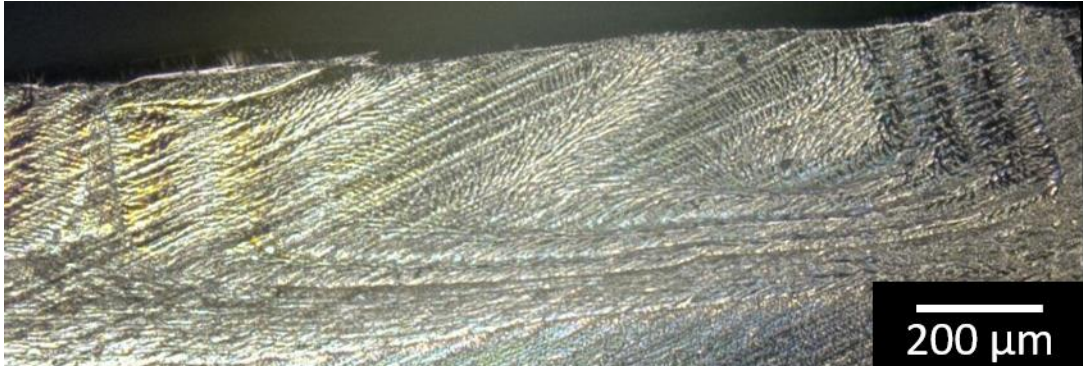


Figure 34. Confocal microscopy image of boxfish scute oblique cross-section. The interfibrillar gaps are shown with a rotation of their longitudinal axis from left to right. Nested-bowl structure only seen near edges where the direction of periodicity (adjacent hexagonal section) changes to orthogonal (in-plane).

5.2 Micro-Computed Tomography

Post-processing sectioning the scute through its thickness reveals, for the first time, a 3D image of the interlaid nested-bowl framework of collagen (Figure 35). Further high resolution μ -CT reveals 3D images of the helical interfibrillar gaps that are similar to those in the twisted plywood, or Bouligand-type, structure of the exoskeleton the lobster *Homarus americanus* [45, 46]. This evidence corroborates research done by Besseau and Bouligand [4] that revealed the twisted plywood (Bouligand-type) structure in the collagen structure of the boxfish. However, this structure is contradictory to the most recent work by Yang et al. [10] that claimed the collagen structure in the boxfish scute follows a ladder-like structure rather than a Bouligand-type structure. That is, that the periodic structure seen on the top surface consists of rows of

collagen planes separated and connected by orthogonal planes acting as the rungs of the ‘ladder’. These claims, although proven here to be false, still demonstrate that this structure consists of a unique type of Bouligand-type arrangement that can easily be confused for a different structure without data to prove otherwise. Moreover, it can be seen in Figure 36b that the apparent rungs of the ladder-like structure are in-fact the helical interfibrillar gaps being exposed. The helical gaps are exposed on the top face when the crack’s width is parallel to the thickness of the dermis and on the front face when the width is orthogonal to the thickness.

μ -CT also provides for clear observation of the mineralized surface plate and collagen base (Figure 35). Measurements through the thickness of the scute reveal that only a mean of 8.5% of the scute thickness is taken by the mineralized plate. The plate itself is considerably thicker at the center of a scute (15% of the thickness) than at the interface (4% of the thickness) due to the raised mineralized surface ridges that extend from the center of the scute to the edges.

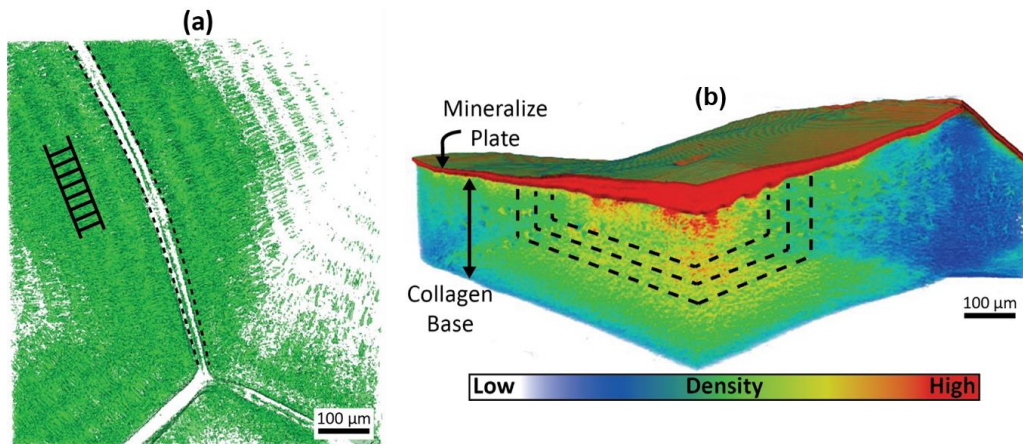


Figure 35. Micro-computed tomography images of boxfish scutes. **(a)** The collagen base displays the periodic structures (ladder representing 180° rotation of collagen planes), but also shows that the interface (outlined) is significantly less dense than the interior of the scute; **(b)** Post-processing sectioning the scute to provide a 3D cross section provides a clear view of the nested-bowl structure and shows that the mineralized plate accounts for a mean of 8.5% thickness of the scute.

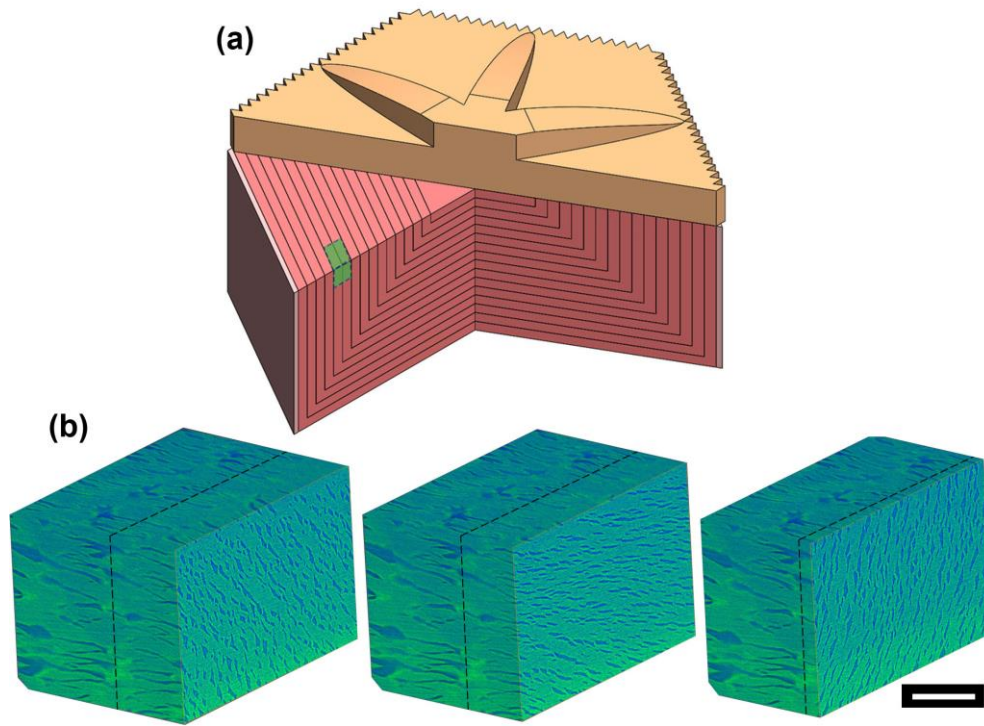


Figure 36. (a) Scute model with highlighted region representing approximate location of the micro-computed tomography (μ -CT) 3D images; (b) Cross sections of 3D μ -CT images showing continuous, helical inter-fibrillar gaps which are representative of a Bouligand-type structure. Dashed black line provides a reference between images and demonstrates the offset of the exposed helical cracks between the top and side faces. That is, the line run in between exposed cracks on top face and between them on bottom face (Scale bar, 100 μ m).

Although the Bouligand-type structure was revealed through the imaging of the helical inter-fibrillar gaps in the top/side regions of the nested bowl structure (Figure 36), these gaps did not appear in the bottom/middle regions where the axis of periodicity changes to become parallel with the dermis. Furthermore, cross-sectional confocal microscopy images (shown in section 5.1) reveal that the pitch length (180° rotation of collagen planes) of this bottom/middle decreases significantly (about 5x smaller). The absence of observable gaps and a decrease in pitch length may suggest this region may have less ductility and more stiffness than the top/side regions.

The boxfish's periodic axis of the Bouligand-type structure and the length of the helical inter-fibrillar gaps align parallel to the outer surface, instead of perpendicular as seen in the

lobster mentioned in the background section (Figure 22). Although further experimentation is needed, this change in helical axis between the boxfish and lobster may highlight that the boxfish is experiencing more in-plane compression due to the bending forces experienced when the boxfish recruits a large portion of its scutes to resist a predator's bite. In other words, the helical axis may be resisting the major axis of compression forces which differs between the lobster and boxfish.

5.3 Nanoindentation

Nanoindentation was performed to further establish whether the collagen of the boxfish scute follows a Bouligand-type structure. Nanoindentation has previously been used as a way of confirming the Bouligand-type structure in other biological materials by quantifying the oscillation of hardness and reduced modulus (stiffness) that is to be expected with a gradual rotation of the anisotropic fibers (i.e. chitin and collagen) [5,40]. Figure 37a represents approximately where the nanoindentation took place and the resultant hardness and reduced modulus maps stitched together from each loading event. There appears to be a gradient running across the length of the maps (Figure 37b and Figure 37c) that may be due to the difficulty in achieving a sufficiently flat surface or from residual mineralization leftover from the polishing of the top mineral plate. A zoom in of the reduced modulus map, shown in Figure 37d, reveals the oscillatory nature of the collagen structure that is to be expected of a Bouligand-type structure along the helical axis. The oscillation between ~20 MPa to ~50 MPa in the reduced modulus may be representative of a gradual oscillation between the transverse and axial moduli of the collagen fibers, respectively. These data corroborate the proposed Bouligand-type structure observed with the 3D imaging of the helical cracks demonstrated in the previous section.

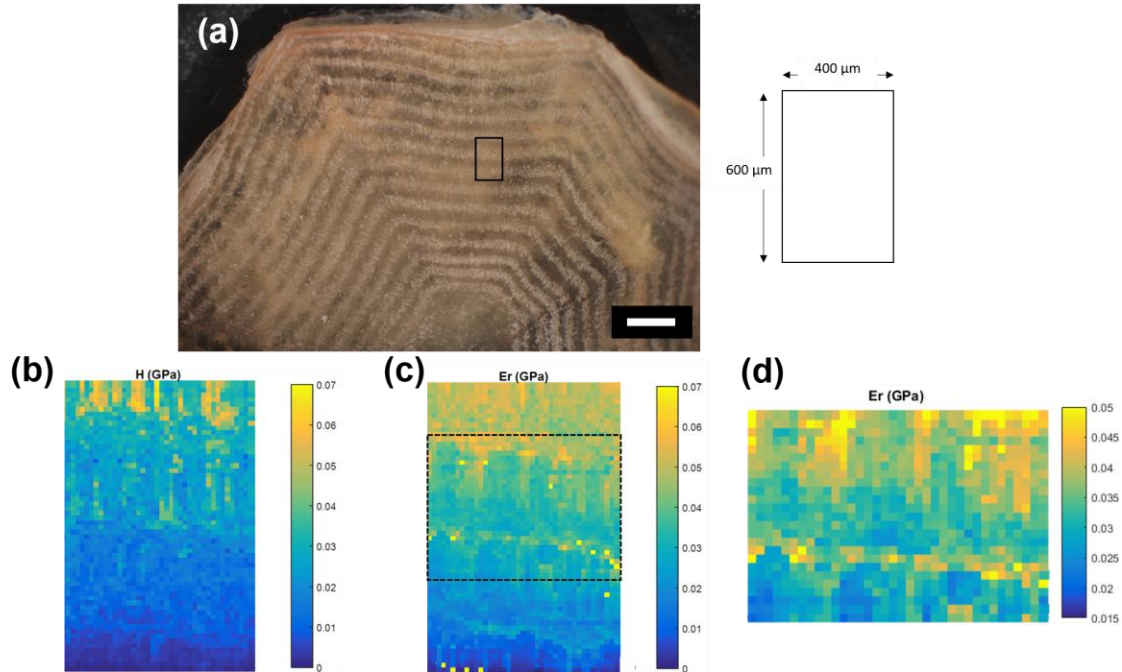


Figure 37. Nanoindentation was performed on the top of a boxfish scute with its mineral plate carefully removed from polishing. **(a)** Image of boxfish scute with approximate location of nanoindentation map, with dimensions of map given on the right, scale bar: 500 μm ; **(b)** Hardness map from nanoindentation; **(c)** Reduced modulus map from nanoindentation with dotted box representing the zoom in, **(d)**. In **(b)** and **(c)** a global gradient is seen in the vertical direction which may be due to the sample being on a slight tilt with respect to the indenter. **(d)** is given to accentuate the oscillation of the reduced modulus, which may be explained by a gradual twisting of collagen fibers.

5.4 *In-situ* Scanning Electron Microscopy

The relatively lower density within the collagen base and small thickness of the mineralized plate both suggest that the interfaces between scutes are more compliant than the scute interior when encountering an applied stress from a predator. To evaluate this, samples were tested with *in situ* SEM mechanical testing to investigate failure. Scutes tested in tension (Figure 38a-b) showed failure occurring entirely at the interface. The mineralized sutures sustain no visible damage and, while some cracks form within the mineralized plate, the collagen base below can be seen to separate and tear (Figure 38b). When tested in a shearing mode (Figure 38c-d) more

damage is visible to the mineralized plate, including the sutures that, in many cases, lock together and fracture. However, final failure still occurs predominantly in the collagen base (Figure 38d).

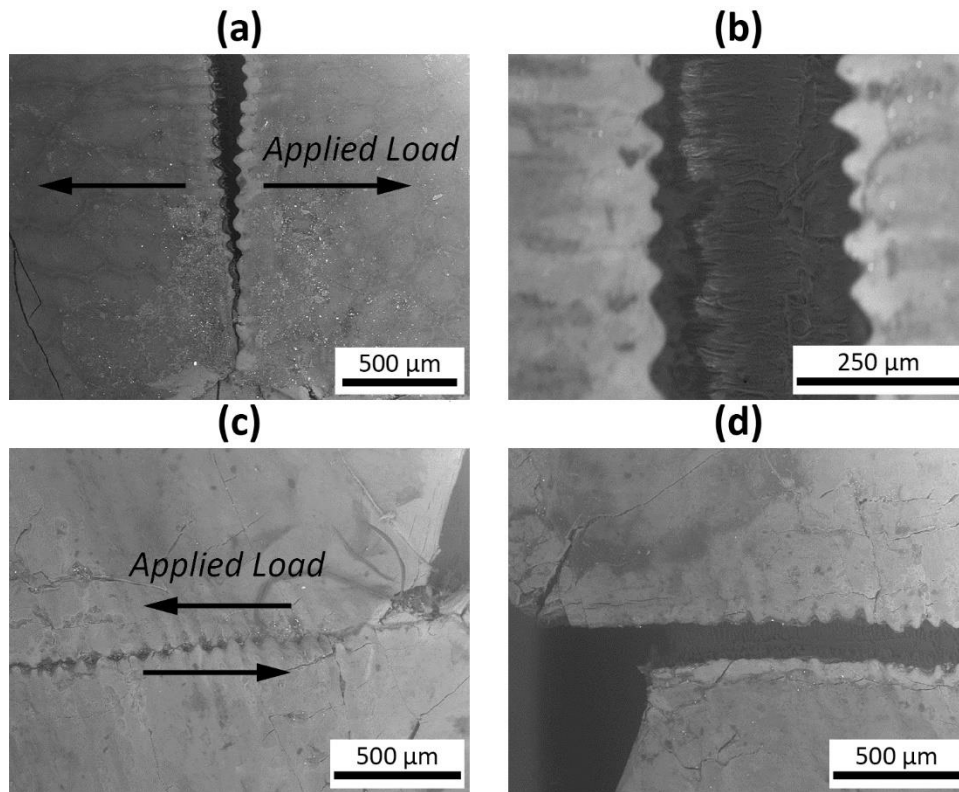


Figure 38. *In situ* scanning electron microscopy images with the mineralized plate under: (a) and (b), tensile loading and (c) and (d), shear loading. (a) In tension little damage to the mineralized plates is observed with the scutes splitting at the interface; (b) close observation of the interface shows no damage to the mineralized sutures, with the collagen base failing underneath; (c) In shear, the mineralized plate experiences more cracking at and near the sutures, however (d) failure occurs again predominantly in the underlying collagen base.

Given that most of the failure occurred in the collagen base but was obscured by the presence of the mineralized plate, *in situ* SEM mechanical testing was performed with the mineralized plate carefully removed. These tests reveal that failure was predominantly located at the interface in both tensile (Figure 39a) and shearing (Figure 39b) loading modes, with minimal damage occurring within the interior collagen of the scute. Consistent failure modes both with and without the presence of the mineralized plate suggest that the mineralized plate's primary purpose does not involve defense against either tension or shear between the scutes. This is generally

consistent with the scales of other fish species, where the outer surface of an individual scale provides a rigid barrier against sharp penetration [42, 43], but the underlying collagen framework provides toughness and ductility through its capacity to sustain plastic deformations [2].

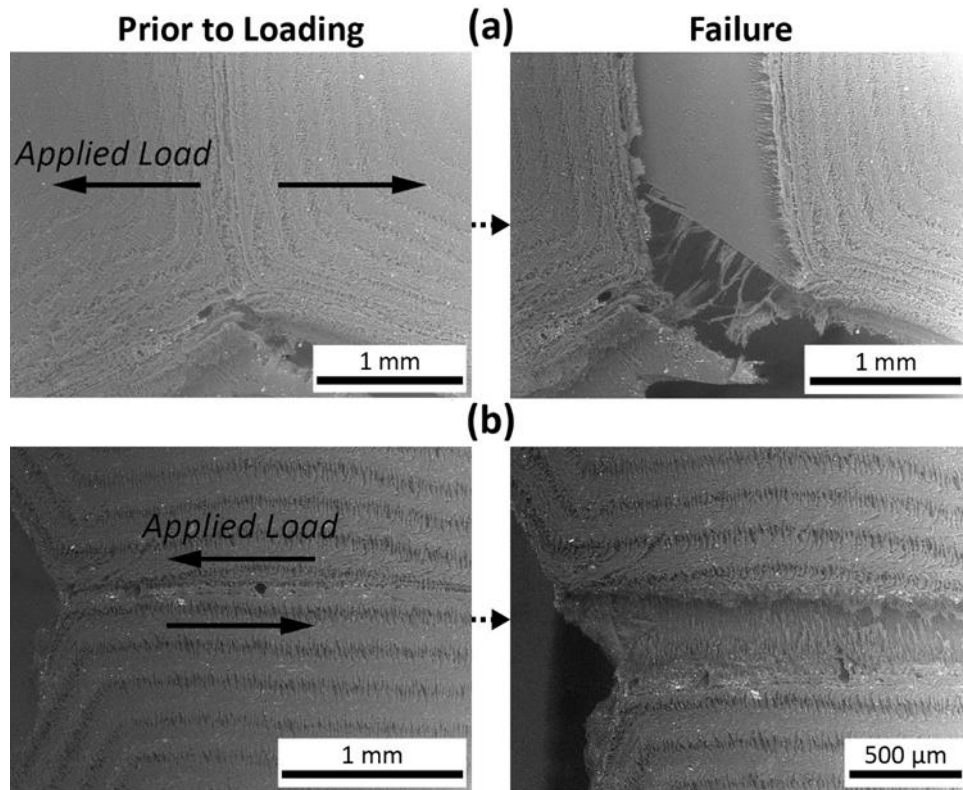


Figure 39. *In situ* scanning electron microscopy images with the mineralized plate removed, loaded in (a) tension and (b) shear. Regardless of the loading mode, failure occurs almost entirely at the interface.

To promote flexibility at the interfaces of the scutes, it is necessary that the interior resist failure and maintains a higher stiffness than the interface. Both the interface and interior are made of the same collagen constituents [10]. Therefore, as is the case of many biological materials [18], the microstructure of the scute's interior must be the source of this increased stiffness.

When observed in SEM, we reveal the periodic resurfacing of the helical cracks as they align orthogonal to the viewed surface (Figure 40a). During *in situ* SEM mechanical loading, these collagen planes deform in a more complex way than expected from straight collagen fibers (Figure

40b). It is proposed that this structure is demonstrating a ductile deformation that allows for the collagen planes to distort and realign with an applied stress, providing some measure of mechanical property isotropy, like other Bouligand-type structures. [2,18]

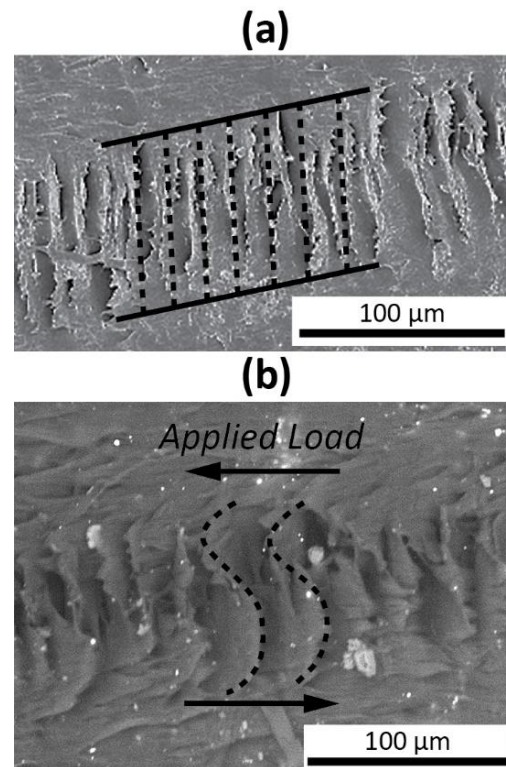


Figure 40. Close-up *in situ* scanning electron microscopy images before and after shear loading; **(a)** The ladder-like structures within the interior of the scute's collagen base consist of collagen planes (dashed lines) that bridge the gap between dense collagen bands (solid lines); **(b)** When a shearing load is applied to this structure, the collagen planes deform into a complex, sinusoidal shape. Images were taken near the interface, but still within the inner region of the scute where the periodic region resides.

Periodic cracking was also observed within one of the pairs of scutes that were tested with the mineral plate removed, as shown in Figure 41. The periodic crack travels through the interface where the angle of the periodic structure of the collagen changes. The crack is periodically exposed which may suggest the crack is following the helical structure of a Bouligand-type structure. That is, as the collagen fibrils within the Bouligand-type structure becoming parallel with the viewed surface the crack (which propagates between collagen fibrils) travels underneath the viewed

surface. This unique crack structure further corroborates that a Bouligand-type structure exists within the collagen structure of the boxfish.

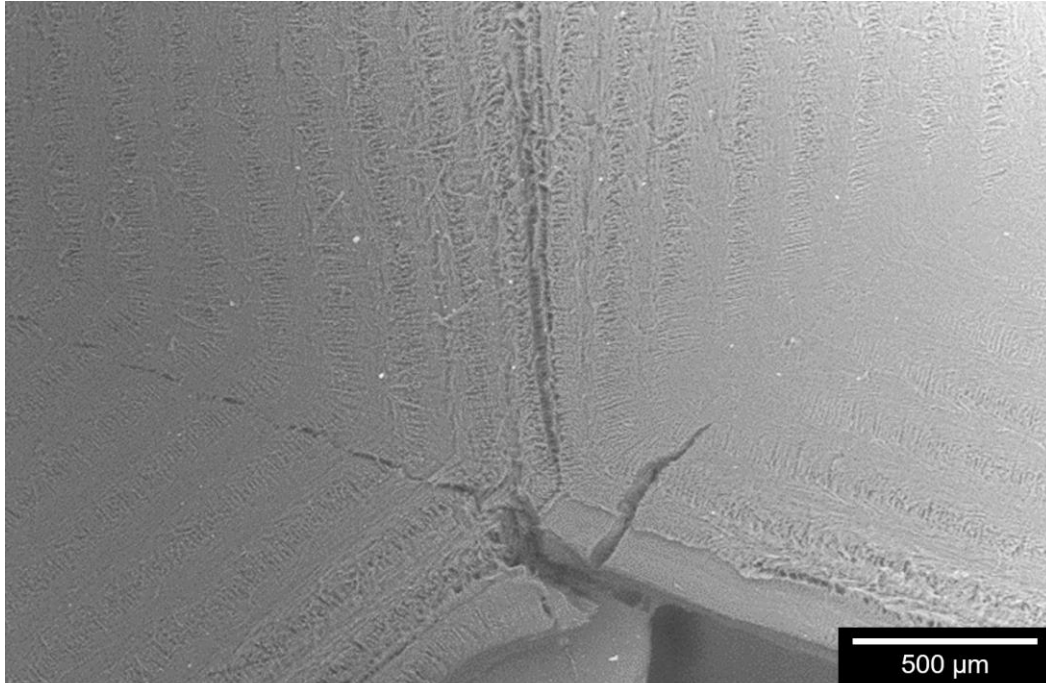


Figure 41. Scanning electron micrograph of neighboring boxfish scutes with mineral plates removed. A periodic crack on left-side scute can be observed which is representative of the periodic Bouligand-type structure of the collagen.

SEM imaging also revealed a unique tubule structure within a crack of the mineral plate in a boxfish scute, as shown in Figure 42. The cracked surface appears to have an array of tubules with material pulled out of them due to the cracking event. It is postulated that these tubules are the product of the transition that takes place to mineralize the collagenous underlayer into the mineral plate. Moreover, the helical interfibrillar gaps in the collagenous underlayer observed in μ -CT are hypothesized to act as ion channels for mineralization processes (like the aforementioned lobster's exoskeleton) [45,46]. This image may be revealing the post-mineralization remnants of the helical gaps.

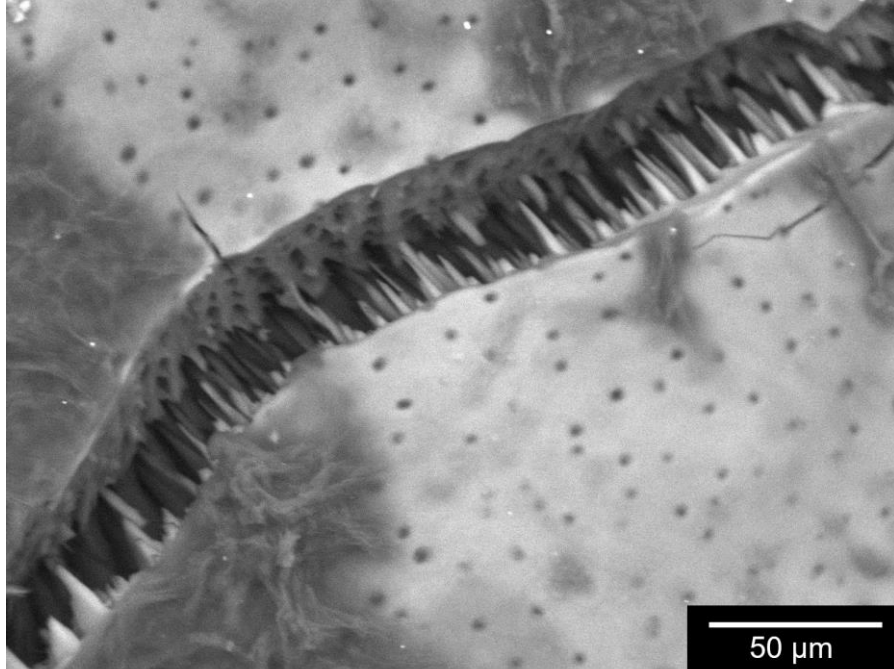


Figure 42. Scanning electron micrograph of crack in the mineral plate of a boxfish scute. Tubules with uncharacterized material extending out.

5.5 In-situ Small Angle X-ray Scattering

In-situ small angle x-ray scattering (SAXS) was done to characterize the collagen structure and mechanics at the interface between neighboring boxfish scutes where the failure has been shown to localize during deformation. The diffraction patterns (Figure 43) featured circular arcs and enlarged dots. The circular arcs are representative of the characteristic d-period within collagen fibrils, while the enlarged dots are representative of the distance between collagen fibrils. A similar pattern is found in the human cornea where enlarged circular patterns are related to the collagen fibril diameter [37]. Measurements of the collagen fibril diameter from SEM done by Yang et al. [10] of 55 ± 10 nm agree closely with measurements taken from SAXS of 53 ± 10 nm, which suggests the collagen fibrils are tightly packed.

Some of the samples tested with SAXS exhibited only one preferential direction of collagen fibrils (Figure 43a) while others demonstrated two preferential direction (Figure 43b).

This was revealed by the existence of either one pair of dots and arcs or two pairs of dots and arcs. The reason for the difference between the samples is unknown but are also shown through scanning electron micrographs taken after deformation, shown in Figure 44. This evidence further suggests that the interfacial collagen between scutes is less structured than the Bouligand-type structure within the interior of the scute, as previously demonstrated with μ -CT and in Yang et al [10].

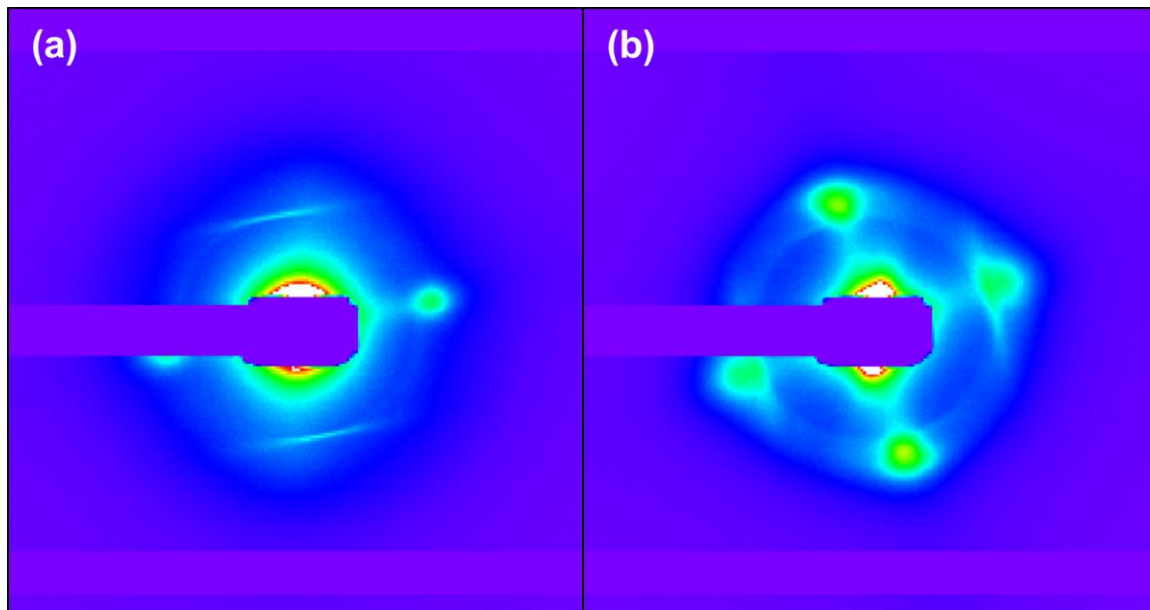


Figure 43. Small angle x-ray scattering patterns obtained from a top-down scan in between two neighboring boxfish scutes before undergoing deformation; **(a)** Reveals one pair of arcs and dots which represents only one preferential direction of collagen fibers; **(b)** Reveals two pairs of arcs and dots which suggests two preferential directions of collagen fibers. It is unknown why some boxfish samples revealed only one distinct preferential direction, while others revealed two. Vertical axes of patterns are the same as tensile axis.

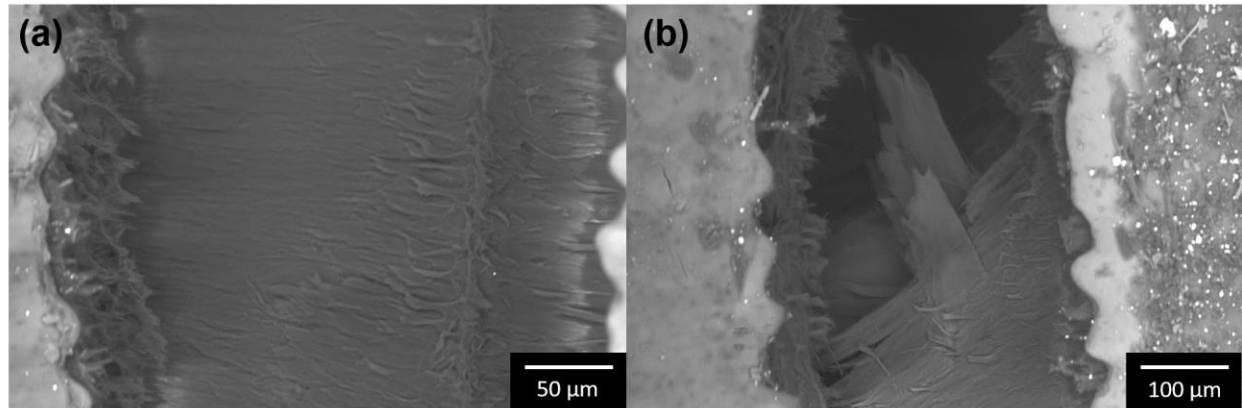


Figure 44. *In-situ* scanning electron microscopy of the collagen fibers at the interface between neighboring boxfish scutes after tensile loading; **(a)** Reveals unidirectional collagen fibers connecting the two neighboring scutes; **(b)** Reveals a pair of orthogonal collagen fibers connecting neighboring scutes at oblique angles. The observance of different architectures corroborates the differences in the structures deduced by the in-situ small angle x-ray scattering patterns on similar boxfish samples.

The pairs of boxfish scutes tested without a mineral plate were analyzed with digital image correlation software that enabled the calculation of the tissue strains by digitally tracking surface features during the deformation. These strains were averaged together and plotted against the measured stresses in both the tensile and shear cases, as shown in Figure 45. Moreover, Figure 45 shows that tissue strains reach values greater than 40% before the failure at the interface occurred, demonstrating a ductile response.

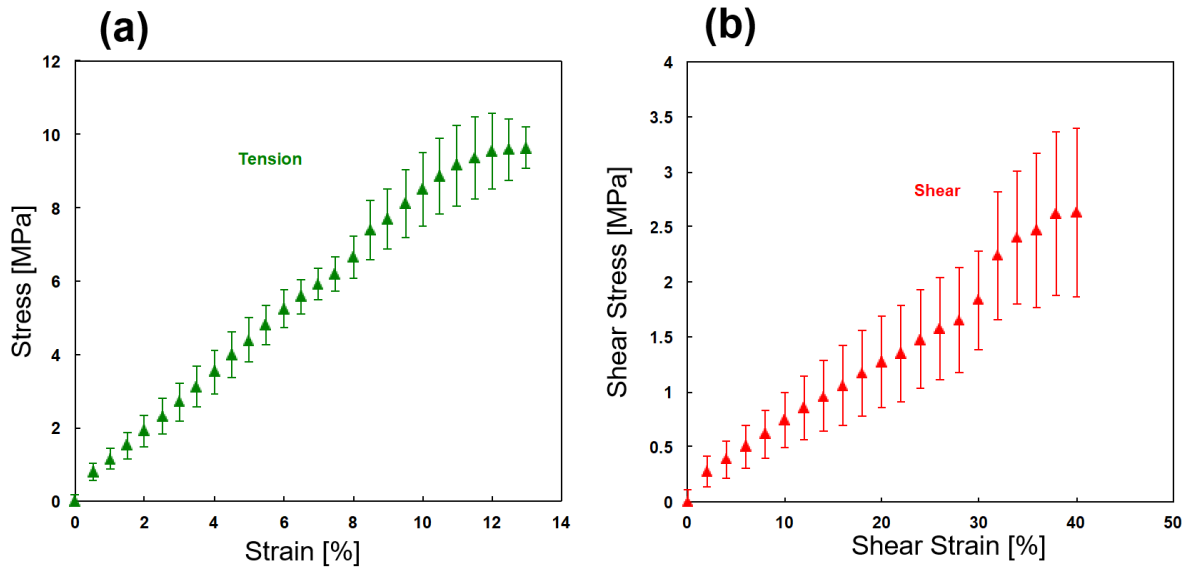


Figure 45. (a) Stress-strain data for the tensile test with two neighboring boxfish scutes with mineral plate removed; (b) Shear stress-shear strain data for the shear test with two neighboring scutes. Significantly higher strains are observed in the shear data, as compared to the tensile data.

By utilizing a combination of digital image correlation and *in-situ* SAXS, the overall tissue strain can be compared to the individual fibril strain as shown in Figure 46. The results demonstrate that the tissue experiences more deformation than the constituent collagen fibrils, as expected. However, it should be noted that in shear (Figure 46b) tissue strains reach strains of 40%, while the fibrils are at a modest 3%. This demonstrates that the structural organization of the collagen fibrils is well suited for a ductile response to shear deformation and could be a major contribution to the overall toughness of the boxfish's dermal armor.

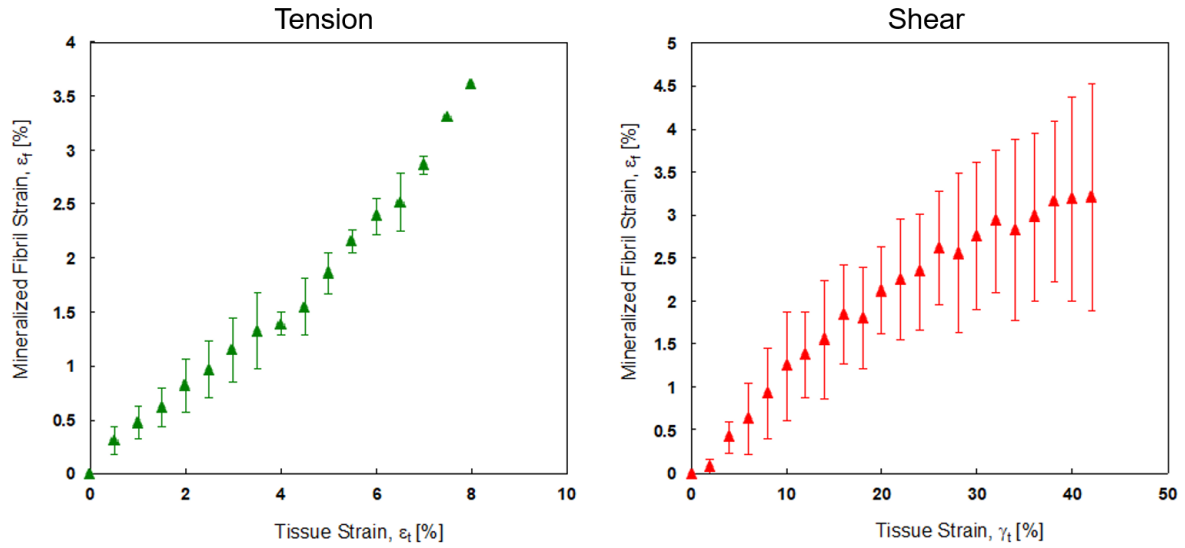


Figure 46. Fibril strain (obtained from in-situ SAXS) versus overall tissue strain (obtained from digital image correlation) of the interfacial collagen between two neighboring boxfish scutes during tension, (a), and shear, (b).

6 Applications and Bio-inspiration

Bioinspired designs of fish scales date back to the Roman Empire with the *Lorica Squamata* which consisted of several overlapping metal scales pinned onto a leather base, creating a composite that can both resist penetration and maintain flexibility for both comfort and toughness, shown in Figure 47 [49].



Figure 47. (a) Mosaic art from about the fourth century B.C. depicting soldiers in Lorica Squamata armor. (b) Archaeological artifact of the Lorica Squamata armor. Images adapted from [49].

Recent studies are now using simulation, 3D printing, and laser engraving, among other technologies, to explore what geometries and properties of scales are needed for various desired properties of the overall composite [50-53].

The scute-style armor of the boxfish, as opposed to the traditional overlapping scales, are now being further investigated for bioinspired applications. Chintapalli et al. (2014) have analyzed the mechanics of an array of hexagonal scutes synthesized from laser engraving a sheet of thin glass laid on top of rubber [52]. They found that the array not only provided more flexibility to the underlying soft substrate, as compared to a thin unengraved glass sheet, but also reduced flexural stresses and delayed fracture of the overall composite. Their results demonstrate

that using the boxfish as a source of bioinspired design can lead to novel designs for various armors for use in soft robotics and flexible electronics, for example.

Aside from the scute structure, the boxfish scute's complex and impact resistant collagen structure can provide inspiration for a new generation of hierarchically organized fiber-reinforced composites. Recent research has been replicating the Bouligand-type structures and have shown promising results [54-57]. For example, F. Pinto et al. (2016) [54] has recreated the Bouligand structure with carbon fiber reinforced polymers and have shown that this structure overcomes the issue of weak out-of-plane properties (e.g. delamination between layers) without significantly degrading the in-plane properties. Another example of mimicking the Bouligand-type structure is done by Greenhall and Raeymaekers [55], where ultrasound is used in combination with stereolithography to direct self-assembly of nano- or microparticles embedded in a polymer matrix, as shown in Figure 48. 3D printing the Bouligand-type structure has also been explored by Yang et al. [56], where nanocomposites are made through electrical assisted assembly of surface modified multiwalled carbon nanotubes (Figure 49).

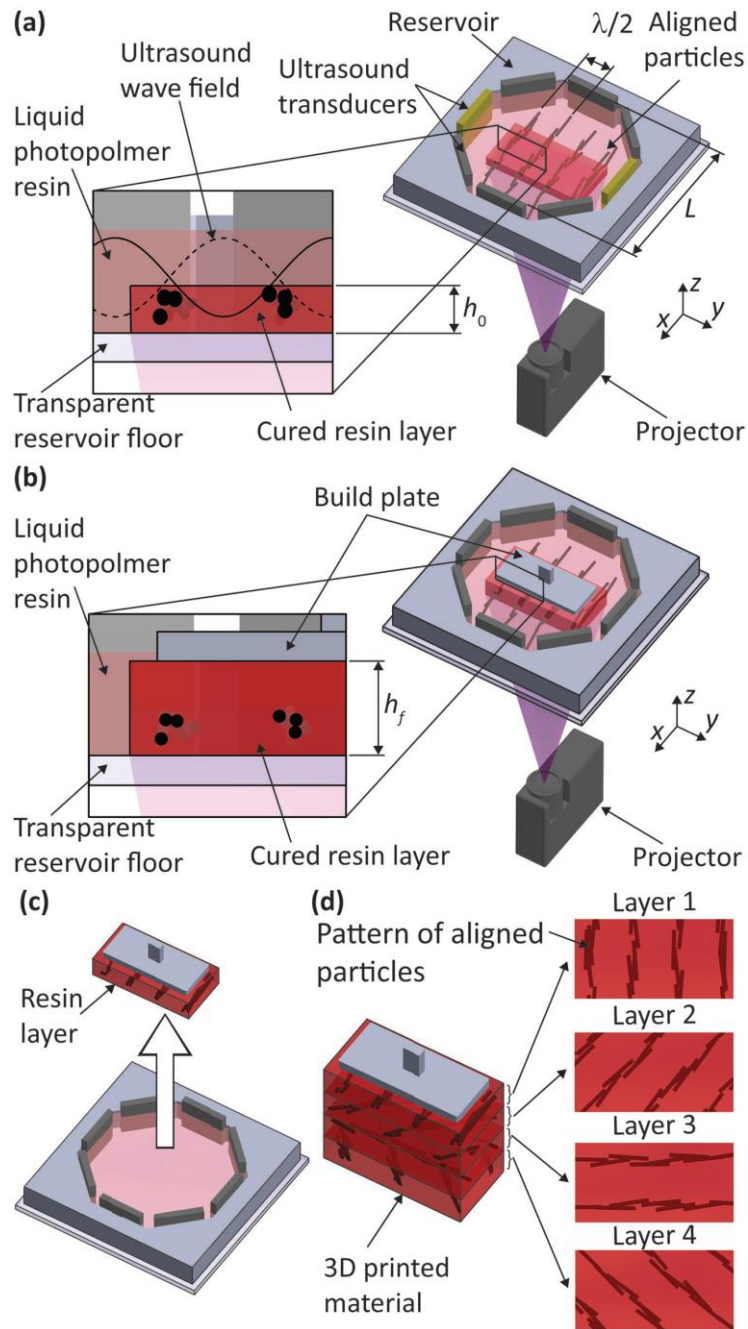


Figure 48. 3D printing of Bouligand-type structural materials through combination of stereolithography and ultrasound directed self-assembly. (a) Ultrasound used to guide the self-assembly of nano- and/or microparticles into lamellar chains; (b) Curing process; (c) Lifting of cured layer to (d) facilitate layer-by-layer control. Figure adapted from [54].

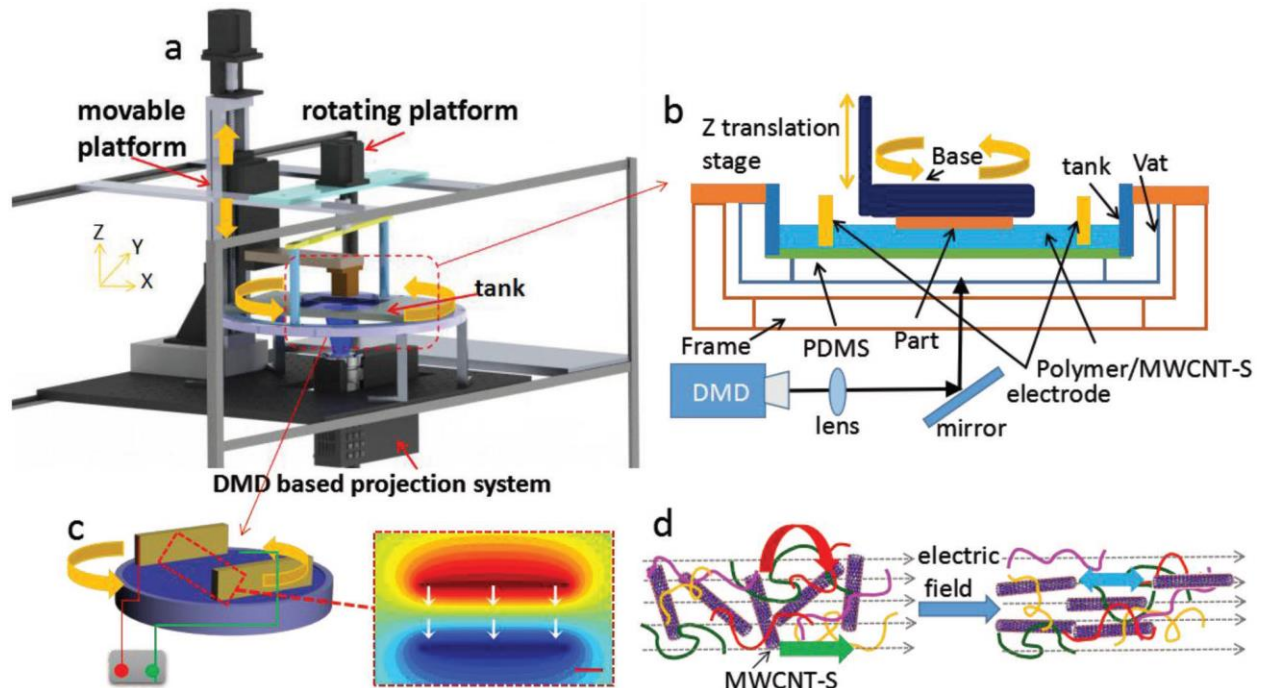


Figure 49. Schematic diagram of the electrically assisted 3D printing platform, (a), for synthesis of Bouligand-type nanostructures with surface modified multiwall carbon nanotubes (MWCNT-S); (b) Bottom-up projection process; (c) Parallel electrode with direct current electric field with accompanied potential simulation; (d) Rotation of MWCNT-S due to electric field. Figure adapted from [55].

Researching involving novel Bouligand-type engineered materials is not confined to biomimicry as utilizing the natural Bouligand-type materials through biotemplating offers a cheap and sustainable alternative for engineering applications. Yao et al. [57] have successfully synthesized nanostructured battery electrodes by performing a biotemplating process on crab shells (Figure 50), which naturally are composed of Bouligand-type arrangements of chitin fibers. The product is a hollow nanofiber electrode for use in rechargeable lithium ion batteries that exhibit high specific capacity and a long cycle life. Whether it is using biomimicry or biotemplating to harness the properties of Bouligand-type structures, there is still much more potential in creating Bouligand-type bioinspired materials, such as using the unique Bouligand-type structure of the boxfish.

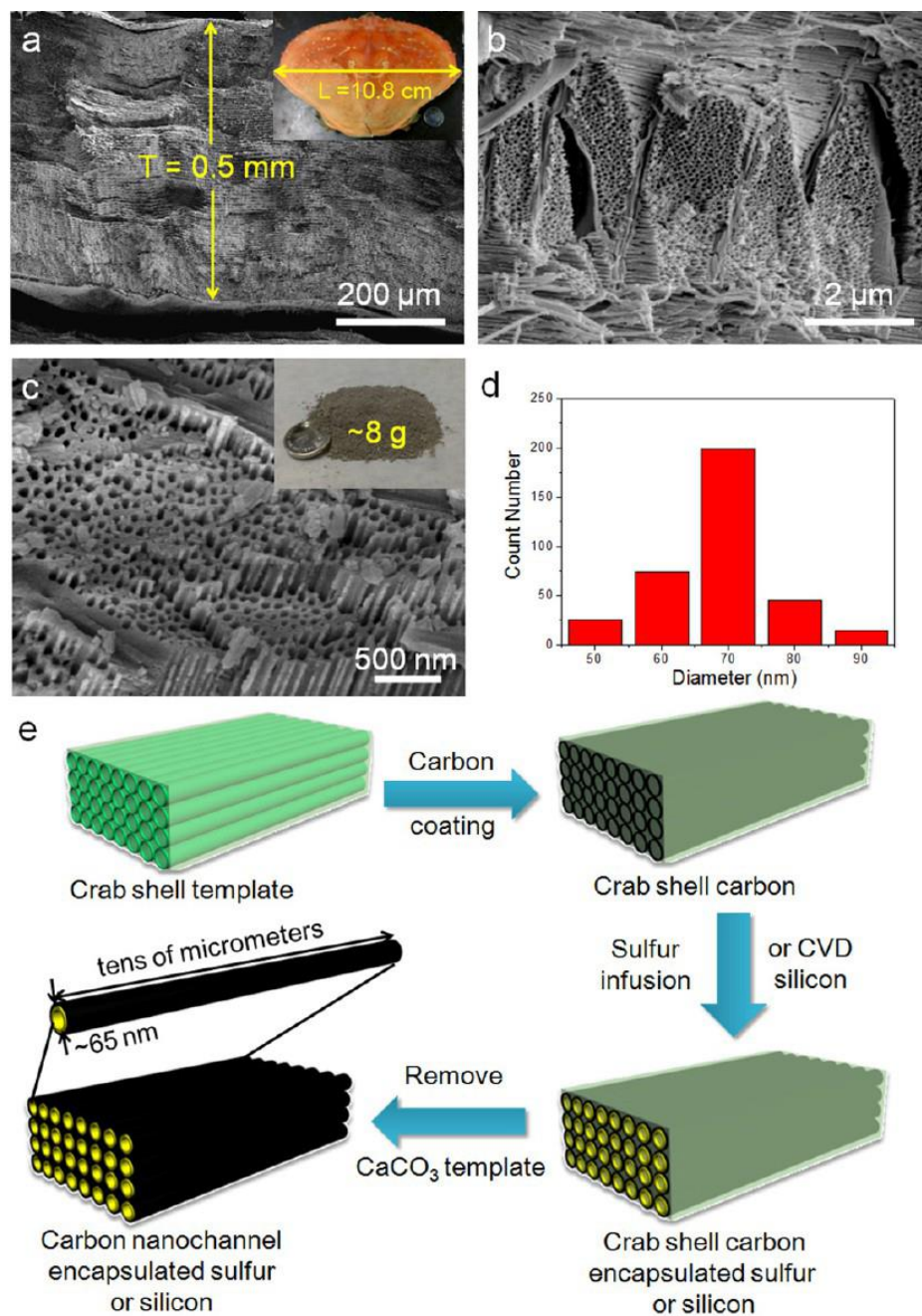


Figure 50. Biotemplating of stone crab shell with Bouligand-type structure. (a-c) Scanning electron micrographs of the cross-section of crab shell, shell template, and powder from template, respectively; (d) Diameter distribution of nanoscale channels; (e) Schematic illustration of the multi-step biotemplating process. Figure adapted from [57].

7 Conclusion

This thesis analyzed the structure and mechanical properties of the dermal armor of the boxfish (*Lactoria cornuta*). The polygonal scutes, which together make-up the dermal armor, were characterized using confocal microscopy, micro-computed tomography (μ -CT), nanoindentation, in-situ scanning electron microscopy (SEM), and small angle x-ray scattering (SAXS).

- Confocal microscopy reveals the overall organization of collagen underneath a boxfish scute. The top-view revealed, as seen in other works, the periodic structure following the polygonal shape of the scute. The cross-sectional images reveal an overall nested-bowl structure that locally is composed of twisted plywood, or Bouligand-type, structures. Furthermore, both top-view and cross-sectional images of the interface between scutes reveals that the interfacial collagen lacks the exposed interfibrillar gaps seen within the nested-bowl structure, suggesting this region is structurally different than the inner collagen.
- μ -CT of the overall scute revealed the significant differences, as expected, between the density of the top mineral plate and the underlying collagen. It also revealed that the plate's thickness, relative to the thickness of the dermis, tapered from 15% to 4% due to the raised mineralized surface ridges that extend from the center of the scute to the edges. This suggests both that most of the mechanical resistance is expected to come from the underlying collagen region, and that the interfaces are designed to be more flexible compared to the center of the scute. Moreover, μ -CT revealed the nested-bowl structure and a difference in density between the collagen at the interfaces between scutes versus within the nested-bowl structure.

- Higher-resolution μ -CT within the periodic region near the top of the scute revealed a multitude of helical interfibrillar gaps. These helical gaps are characteristic of a Bouligand-type structure as they represent interfibrillar gaps which rotate to follow the rotation of the collagen planes; thereby, corroborating that this complex collagen structure is of the Bouligand-type.
- Nanoindentation was performed to quantify the oscillation in hardness and reduced modulus that is to be expected with rotating fibers. Results demonstrated there is an oscillation between ~ 20 MPa and ~ 50 MPa in the reduced modulus which represent the change in the transverse and axial moduli of the collagen fibers, respectively.
- *In-situ* SEM was used to observe the deformation response of two-adjacent scutes (with and without the mineral plate) to both tensile and shear testing. All samples failed predominantly at the interface between adjacent scutes suggesting that this interfacial region is designed to preferentially absorb energy to protect the inner region from deformation. Samples with the mineral plate removed were imaged using the SEM before and after deformation and revealed that collagen is capable of deforming to align with the applied force to provide damage resistance, as seen in other biological materials with a Bouligand-type structure.
- SAXS revealed that the interfacial collagen fibrils between neighboring scutes can consist of either one or two preferential directions and further confirms the structure within this region is less complex and ductile with respect to the Bouligand-type structure within the interior of the scute.

To revisit the hypothesis of this thesis, the work here suggests that there is a Bouligand-type structure present within the collagen of a boxfish scute. This conclusion disagrees with

previous results from Wen et al. [10] which claimed there was not a Bouligand-type structure present. The use of μ -CT in this work allowed for a 3-dimensional look into this complex structure and revealed a network of helical gaps which indirectly suggest the presence of a Bouligand-type structure. This hypothesis was further demonstrated by the oscillation observed in the reduced modulus and hardness maps obtained from nanoindentation which represent the rotation of the collagen fibers in a Bouligand-type structure. Finally, the localization of failure within the interfacial regions and deformation of the inner collagen to align with the loading conditions during *in-situ* SEM reveal efficient damage-control mechanisms of the boxfish's dermal armor.

7.1 Recommendations for Future Research

Future research on the boxfish should take multiple fronts that serve to: (1) further the understanding of the mechanics of the boxfish's dermal armor; (2) explore bioinspired designs to determine optimal design parameters; (3) testing of bioinspired designs for various applications including armors for soft robotics, flexible electronic designs, and novel fiber reinforced materials. Both the unique mineral structure of hexagonal scutes with sutured interfaces as well as the unique Bouligand-type structure in the collagen base provide outlets for further bioinspired design. Examples of future work include:

- Using finite element simulations and bioinspired sutured composites under shear loading to further the understanding of the composite's crack mechanics when the sutured teeth are interlocked to explore the mechanical efficiency of composites with sutured interfaces.
- Testing array of boxfish scutes under bending conditions that are similar to the bending caused by predator's bites (with and without mineral plates removed) and

further continuing similar experiments with bioinspired composites and finite element modelling to observe the role of the hexagonal scutes in resisting concave bending while retaining modest flexibility.

- Exploring and analyzing Bouligand-type structures using 3D printed specimens under various loading conditions that include the helical interfibrillar gaps found in the boxfish and lobster. This work may confirm the mechanical utility offered by these gaps and can also provide inspiration for novel self-healing fiber reinforced composites that utilize the gaps for both material transport and mechanical efficiency.
- Performing more *in-situ* SAXS on isolated sections of the boxfish scute. This will potentially reveal the Bouligand-type structure in both the upper/side and lower/mid regions and how they differ in both structure and mechanical response.

Appendix

Appendix A. Staining Protocol

- * Boxfish scute was prepared similarly as previously described in Bushong et al. [53].
- * Stained samples were used in both the confocal microscopy and micro-computed tomography.
 1. The scutes were carefully cut with scalpel from boxfish specimen (*Lactoria cornuta*).
 2. The scutes were washed with buffer and then placed into 2% OsO₄ with 1.5% potassium ferrocyanide in 0.15 M cacodylate buffer containing 2 mM CaCl₂.
 3. The scutes were left for 30 minutes on ice.
 4. The scute were left for 30 minutes at room temperature.
 5. The scutes were thoroughly washed in double distilled water.
 6. The scutes were placed into 0.5% thiocarbohydrazide for 30 minutes.
 7. The scutes were again washed in double distilled water.
 8. The scute were then stained with 2% aqueous OsO₄ for 30 minutes.
 9. The scutes were washed and then placed into 2% aqueous uranyl acetate overnight at 4°C.
 10. The scutes were washed with water at room temperature and then stained with en bloc lead aspartate for 30 minutes at 60°C.
 11. The scutes were washed with water and then dehydrated on ice in 70, 90, 100% ethanol solutions for 10 minutes at each step.
 12. The scutes were then washed twice in dry acetone and then placed into 50:50 Durcupan ACM:acetone overnight.

13. The scutes were transferred to 100% Durcupan resin overnight in a vacuum chamber.
14. The scutes were then flat embedded between glass slides coated with mould-release compound and left in an oven at 60°C for 48 h.

Appendix B. Rehydration of Boxfish Scutes Protocol

- * Boxfish scutes were originally preserved in a semi-dehydrated state (1:1 by volume of isopropanol and deionized water).
- * Rehydration was done for *in-situ* scanning electron microscopy and nanoindentation.
 1. The scutes were removed from preserved semi-dehydrated solution and placed into a solution containing 1:2 by volume of isopropanol and Hank's Balanced Salt Solution (electrolyte water). Scutes were left in solution for 30 minutes.
 2. Step 1 was then repeated with the following solutions, 30 minutes each:
 - a. 1:3 isopropanol/Hank's Balanced Salt Solution
 - b. 1:9 isopropanol/Hank's Balanced Salt Solution
 3. The scutes were then placed in 100% Hank's Balanced Salt Solution for 24 hours before testing.

This thesis, in full, is currently being prepared for submission for publication of the material. Garner, Sean; Naleway, Steven; Housseini, Maryam; Acevedo, Claire; Gludovatz, Bernd; Schaible, Eric; McKittrick, Joanna; Zavattieri, Pablo.

References

- [1] Porter, M. M., Ravikumar, N., Barthelat, F., & Martini, R. (2017). 3D-printing and mechanics of bio-inspired articulated and multi-material structures. *Journal of the Mechanical Behavior of Biomedical Materials*, 73, 114-126. doi:10.1016/j.jmbbm.2016.12.016
- [2] Zimmermann, E. A., Gludovatz, B., Schaible, E., Dave, N. K., Yang, W., Meyers, M. A., & Ritchie, R. O. (2013). Mechanical adaptability of the Bouligand-type structure in natural dermal armour. *Nature Communications*, 4(1). doi:10.1038/ncomms3634
- [3] Suksangpanya, N., Yaraghi, N. A., Kisailus, D., & Zavattieri, P. (2017). Twisting cracks in Bouligand structures. *Journal of the Mechanical Behavior of Biomedical Materials*, 76, 38-57. doi:10.1016/j.jmbbm.2017.06.010
- [4] Besseau, L., & Bouligand, Y. (1998). The twisted collagen network of the box-fish scutes. *Tissue and Cell*, 30(2), 251-260. doi:10.1016/s0040-8166(98)80073-6
- [5] Yang, R., Zaheri, A., Gao, W., Hayashi, C., & Espinosa, H. D. (2017). Exoskeletons: AFM Identification of Beetle Exocuticle: Bouligand Structure and Nanofiber Anisotropic Elastic Properties (Adv. Funct. Mater. 6/2017). *Advanced Functional Materials*, 27(6). doi:10.1002/adfm.201770031
- [6] Feilden, E., Ferraro, C., Zhang, Q., García-Tuñón, E., D'Elia, E., Giuliani, F., Vandeperre, L., Saiz, E. (2017). 3D Printing Bioinspired Ceramic Composites. *Scientific Reports*, 7(1). doi:10.1038/s41598-017-14236-9
- [7] Natarajan, B., Krishnamurthy, A., Qin, X., Emiroglu, C. D., Forster, A., Foster, E. J., Weder, C., Fox, D. M., Keten, S., Obrzut, J., Gilman, J. W. (2018). Binary Cellulose Nanocrystal Blends for Bioinspired Damage Tolerant Photonic Films. *Advanced Functional Materials*, 28(26), 1800032. doi:10.1002/adfm.201800032
- [8] Nguyen, T., Peres, B. U., Carvalho, R. M., & Maclachlan, M. J. (2016). Photonic Hydrogels from Chiral Nematic Mesoporous Chitosan Nanofibril Assemblies. *Advanced Functional Materials*, 26(17), 2875-2881. doi:10.1002/adfm.201505032
- [9] Sharma, V., Crne, M., Park, J. O., & Srinivasarao, M. (2014). Bouligand Structures Underlie Circularly Polarized Iridescence of Scarab Beetles: A Closer View. *Materials Today: Proceedings*, 1, 161-171. doi:10.1016/j.matpr.2014.09.019
- [10] Yang, W., Naleway, S. E., Porter, M. M., Meyers, M. A., & McKittrick, J. (2015). The armored carapace of the boxfish. *Acta Biomaterialia*, 23, 1-10. doi:10.1016/j.actbio.2015.05.024
- [11] Santini, F., Sorenson, L., Marcroft, T., Dornburg, A., & Alfaro, M. E. (2013). A

- multilocus molecular phylogeny of boxfishes (Araucanidae, Ostraciidae; Tetraodontiformes). *Molecular Phylogenetics and Evolution*, 66(1), 153-160. doi:10.1016/j.ympev.2012.09.022
- [12] Bartol, I. K. (2005). Body-induced vortical flows: A common mechanism for self-corrective trimming control in boxfishes. *Journal of Experimental Biology*, 208(2), 327-344. doi:10.1242/jeb.01356
- [13] Wassenbergh, S. V., Manen, K. V., Marcroft, T. A., Alfaro, M. E., & Stamhuis, E. J. (2014). Boxfish swimming paradox resolved: Forces by the flow of water around the body promote manoeuvrability. *Journal of The Royal Society Interface*, 12(103), 20141146-20141146. doi:10.1098/rsif.2014.1146
- [14] I.K. Bartol, M. Gharib, D. Weihs, P.W. Webb, J.R. Hove, M.S. Gordon, Hydrodynamic stability of swimming in ostraciid fishes: role of the carapace in the smooth trunkfish *Lactophrys triqueter* (Teleostei: Ostraciidae), *J. Exp. Biol.* 206 (2003) 725–744.
- [15] I.K. Bartol, M.S. Gordon, M. Gharib, J.R. Hove, P.W. Webb, D. Weihs, Flow patterns around the carapaces of rigid-bodied, multi-propulsor boxfishes (Teleostei: Ostraciidae), *Integr. Comp. Biol.* 42 (2002) 971–980.
- [16] M. Gharib, F. Pereira, D. Dabiri, J.R. Hove, D. Modarress, Quantitative flow visualization: toward a comprehensive flow diagnostic tool, *Integr. Comp. Biol.* 42 (2002) 964–970.
- [17] M.S. Gordon, J.R. Hove, P.W. Webb, D. Weihs, Boxfishes as unusually wellcontrolled autonomous underwater vehicles, *Physiol. Biochem. Zool.* 73 (2000) 663–671.
- [18] Naleway, S. E., Porter, M. M., McKittrick, J., & Meyers, M. A. (2015). Structural Design Elements in Biological Materials: Application to Bioinspiration. *Advanced Materials*, 27(37), 5455-5476. doi:10.1002/adma.201502403
- [19] Li, Y., Ortiz, C., & Boyce, M. C. (2013). A generalized mechanical model for suture interfaces of arbitrary geometry. *Journal of the Mechanics and Physics of Solids*, 61(4), 1144-1167. doi:10.1016/j.jmps.2012.10.004
- [20] Malik, I. A., & Barthelat, F. (2018). Bioinspired sutured materials for strength and toughness: Pullout mechanisms and geometric enrichments. *International Journal of Solids and Structures*, 138, 118-133. doi:10.1016/j.ijsolstr.2018.01.004
- [21] Lin, E., Li, Y., Weaver, J. C., Ortiz, C., & Boyce, M. C. (2014). Tunability and enhancement of mechanical behavior with additively manufactured bio-inspired hierarchical suture interfaces. *Journal of Materials Research*, 29(17), 1867-1875. doi:10.1557/jmr.2014.175

- [22] Lin, E., Li, Y., Ortiz, C., & Boyce, M. C. (2014). 3D printed, bio-inspired prototypes and analytical models for structured suture interfaces with geometrically-tuned deformation and failure behavior. *Journal of the Mechanics and Physics of Solids*, 73, 166-182. doi:10.1016/j.jmps.2014.08.011
- [23] Li, Y., Ortiz, C., & Boyce, M. C. (2011). Stiffness and strength of suture joints in nature. *Physical Review E*, 84(6). doi:10.1103/physreve.84.062904
- [24] Haydn N. G. Wadley (2006). Multifunctional periodic cellular metals. *Phil. Trans. R. Soc. A*, 364, 31-68. doi:10.1098/rsta.2005.1697
- [25] Birman, V., & Kardomateas, G. A. (2018). Review of current trends in research and applications of sandwich structures. *Composites Part B: Engineering*, 142, 221-240. doi:10.1016/j.compositesb.2018.01.027
- [26] Sabah, S. A., Kueh, A., & Al-Fasih, M. (2017). Comparative low-velocity impact behavior of bio-inspired and conventional sandwich composite beams. *Composites Science and Technology*, 149, 64-74. doi:10.1016/j.compscitech.2017.06.014
- [27] Yang, X., Ma, J., Shi, Y., Sun, Y., & Yang, J. (2017). Crashworthiness investigation of the bio-inspired bi-directionally corrugated core sandwich panel under quasi-static crushing load. *Materials & Design*, 135, 275-290. doi:10.1016/j.matdes.2017.09.040
- [28] Fratzl, P., & Gupta, H. S. (2007). Nanoscale Mechanisms of Bone Deformation and Fracture. *Handbook of Biomineralization*, 397-414. doi:10.1002/9783527619443.ch23
- [29] Fratzl, P., & Weinkamer, R. (2007). Nature's hierarchical materials. *Progress in Materials Science*, 52, 1263-1334. doi:10.1016/j.pmatsci.2007.06.001
- [30] Gupta, H. S., Seto, J., Wagermaier W., Zaslansky, P., Boesecke, P., Fratzl, P. (2006). Cooperative deformation of mineral and collagen in bone at the nanoscale. *Proceeding of the National Academy of Sciences*, 103, 17741-17746. doi:10.1073/pnas.0604237103
- [31] Zhang, F., & Ilavsky, J. (2010). Ultra-Small-Angle X-ray Scattering of Polymers. *Polymer Reviews*, 50(1), 59-90. doi:10.1080/15583720903503486
- [32] Barnard, H. S., Macdowell, A., Parkinson, D., Mandal, P., Czabaj, M., Gao, Y., Maillet, E., Blank, B., Larson, N.M., Ritchie, R. O., Gludovatz, B., Acevado, C., Liu, D. (2017). Synchrotron X-ray micro-tomography at the Advanced Light Source: Developments in high-temperature in-situ mechanical testing. *Journal of Physics: Conference Series*, 849, 012043. doi:10.1088/1742-6596/849/1/012043
- [33] Bernadó, P., Mylonas, E., Petoukhov, M. V., Blackledge, M., & Svergun, D. I. (2007). Structural Characterization of Flexible Proteins Using Small-Angle X-ray Scattering. *Journal of the American Chemical Society*, 129(17), 5656-5664. doi:10.1021/ja069124n

- [34] Zimmermann, E. A., Gludovatz, B., Schaible, E., Busse, B., & Ritchie, R. O. (2014). Fracture resistance of human cortical bone across multiple length-scales at physiological strain rates. *Biomaterials*, 35(21), 5472-5481. doi:10.1016/j.biomaterials.2014.03.066
- [35] Zimmermann, E. A., Schaible, E., Gludovatz, B., Schmidt, F. N., Riedel, C., Krause, M., Vettorazzi, E., Acevado, C., Hahn, M., Puschel, K., Tang, S., Amling, M., Ritchie, R. O., Busse, B. (2016). Intrinsic mechanical behavior of femoral cortical bone in young, osteoporotic and bisphosphonate-treated individuals in low- and high energy fracture conditions. *Scientific Reports*, 6(1). doi:10.1038/srep21072
- [36] Vordos, N., Drosos, G., Kazanidis, I., Ververidis, A., Ypsilantis, P., Kazakos, K., Simopoulos, C., Mitropoulos, A. Ch., Touloupidis, S. (2018). Hydroxyapatite Crystal Thickness and Buckling Phenomenon in Bone Nanostructure During Mechanical Tests. *Annals of Biomedical Engineering*, 46(4), 627-639. doi:10.1007/s10439-018-1983-0
- [37] Quantock, A. J., Boote, C., Young, R. D., Hayes, S., Tanioka, H., Kawasaki, S., Ohta, N., Iida, T., Yagi, N., Kinoshita, S., Meek, K. M. (2007). Small-angle fibre diffraction studies of corneal matrix structure: A depth-profiled investigation of the human eye-bank cornea. *Journal of Applied Crystallography*, 40(S1). doi:10.1107/s0021889807005523
- [38] Bigi, A., Burghammer, M., Falconi, R., Koch, M. H., Panzavolta, S., & Riekel, C. (2001). Twisted Plywood Pattern of Collagen Fibrils in Teleost Scales: An X-ray Diffraction Investigation. *Journal of Structural Biology*, 136(2), 137-143. doi:10.1006/jsbi.2001.4426
- [39] Yaraghi, N. A., Guarín-Zapata, N., Grunenfelder, L. K., Hintsala, E., Bhowmick, S., Hiller, J. M., Betts, M., Principe, E.L., Jung, J.Y., Sheppard, L, Wuhner, R., McKittrick, J., Zavattieri, P., Kisailus, D. (2016). Biocomposites: A Sinusoidally Architected Helicoidal Biocomposite (Adv. Mater. 32/2016). *Advanced Materials*, 28(32), 6769-6769. doi:10.1002/adma.201670219
- [40] Weaver, J. C., Milliron, G. W., Miserez, A., Evans-Lutterodt, K., Herrera, S., Gallana, I., Mershon, W.J., Swanson, B., Zavattieri, P., Dimasi, E., Kisailus, D. (2012). The Stomatopod Dactyl Club: A Formidable Damage-Tolerant Biological Hammer. *Science*, 336(6086), 1275-1280. doi:10.1126/science.1218764
- [41] Zhu D, Ortega CF, Motamedi R, Szewciw L, Vernerey F, Barthelat F. "Structure and mechanical performance of a "modern" fish scale." *Advanced Engineering Materials* (2012);**14**:B185-B194.
- [42] Zhu DJ, Szewciw L, Vernerey F, Barthelat F. "Puncture resistance of the scaled skin from striped bass: Collective mechanisms and inspiration for new flexible armor designs " *Journal of the Mechanical Behavior of Biomedical Materials* (2013);**24**:30-40.
- [43] Varga, P., Pacureanu, A., Langer, M., Suhonen, H., Hesse, B., Grimal, Q., Cloetens, P., Raum, K., Peyrin, F. (2013). Investigation of the three-dimensional orientation of mineralized collagen fibrils in human lamellar bone using synchrotron X-ray phase nanotomography. *Acta Biomaterialia*, 9(9), 8118-8127. doi:10.1016/j.actbio.2013.05.015

- [44] Romano, P., Fabritius, H., & Raabe, D. (2007). The exoskeleton of the lobster *Homarus americanus* as an example of a smart anisotropic biological material. *Acta Biomaterialia*, 3(3), 301-309. doi:10.1016/j.actbio.2006.10.003
- [45] Raabe, D., Romano, P., Sachs, C., Al-Sawalmih, A., Brokmeier, H., Yi, S., Servos, G., Hartwig, H. (2005). Discovery of a honeycomb structure in the twisted plywood patterns of fibrous biological nanocomposite tissue. *Journal of Crystal Growth*, 283(1-2), 1-7. doi:10.1016/j.jcrysgro.2005.05.077
- [46] Sherman, V. R., Quan, H., Yang, W., Ritchie, R. O., & Meyers, M. A. (2017). A comparative study of piscine defense: The scales of *Arapaima gigas*, *Latimeria chalumnae* and *Atractosteus spatula*. *Journal of the Mechanical Behavior of Biomedical Materials*, 73, 1-16. doi:10.1016/j.jmbbm.2016.10.001
- [47] Oliver, W., & Pharr, G. (1992). An improved technique for determining hardness and elastic modulus using load and displacement sensing indentation experiments. *Journal of Materials Research*, 7(06), 1564-1583. doi:10.1557/jmr.1992.1564
- [48] Ehrlich, H. (2015). *Biological materials of marine origin: Vertebrates*. Dordrecht: Springer.
- [49] Martini, R., & Barthelat, F. (2016). Stretch-and-release fabrication, testing and optimization of a flexible ceramic armor inspired from fish scales. *Bioinspiration & Biomimetics*, 11(6), 066001. doi:10.1088/1748-3190/11/6/066001
- [50] Martini, R., Balit, Y., & Barthelat, F. (2017). A comparative study of bio-inspired protective scales using 3D printing and mechanical testing. *Acta Biomaterialia*, 55, 360-372. doi:10.1016/j.actbio.2017.03.025
- [51] Chintapalli, R. K., Mirkhalaf, M., Dastjerdi, A. K., & Barthelat, F. (2014). Fabrication, testing and modeling of a new flexible armor inspired from natural fish scales and osteoderms. *Bioinspiration & Biomimetics*, 9(3), 036005. doi:10.1088/1748-3182/9/3/036005
- [52] Song, J., Ortiz, C., & Boyce, M. C. (2011). Threat-protection mechanics of an armored fish. *Journal of the Mechanical Behavior of Biomedical Materials*, 4(5), 699-712. doi:10.1016/j.jmbbm.2010.11.011
- [53] Pinto, F., Iervolino, O., Scarselli, G., Ginzburg, D., & Meo, M. (2016). Bioinspired twisted composites based on Bouligand structures. *Bioinspiration, Biomimetics, and Bioreplication 2016*. doi:10.1117/12.2219088
- [54] Greenhall, J., & Raeymaekers, B. (2017). 3D Printing Macroscale Engineered Materials Using Ultrasound Directed Self-Assembly and Stereolithography. *Advanced Materials Technologies*, 2(9), 1700122. doi:10.1002/admt.201700122

- [55] Yang, Y., Chen, Z., Song, X., Zhang, Z., Zhang, J., Shung, K. K., Zhou, Q., Chen, Y. (2017). Biomimetics: Biomimetic Anisotropic Reinforcement Architectures by Electrically Assisted Nanocomposite 3D Printing (Adv. Mater. 11/2017). *Advanced Materials*, 29(11). doi:10.1002/adma.201770076
- [56] Yao, H., Zheng, G., Li, W., McDowell, M. T., Seh, Z., Liu, N., Lu, Z., Cui, Y. (2013). Crab Shells as Sustainable Templates from Nature for Nanostructured Battery Electrodes. *Nano Letters*, 13(7), 3385-3390. doi:10.1021/nl401729r
- [57] Bushong, E. A., Johnson, D. D., Kim, K., Terada, M., Hatori, M., Peltier, S. T., Panda, S., Markle, A., Ellisman, M. H. (2014). X-Ray Microscopy as an Approach to Increasing Accuracy and Efficiency of Serial Block-Face Imaging for Correlated Light and Electron Microscopy of Biological Specimens. *Microscopy and Microanalysis*, 21(01), 231-238. doi:10.1017/s1431927614013579